ACADEMIA DA FORÇA AÉREA

Hydrogen Fuel Cell for Unmanned Aerial Systems: Operational Environment Contamination Response

José Guilherme Costa Moura

ASPAL/PILAV 140664-H

Dissertation to obtain the Master of Science Degree in

Military and Aeronautical Sciences – Aviator Pilot

Examination Committee

Chairperson:	BGEN/ENGAER João Rui Ramos Nogueira
Supervisor:	MAJ/ENGAER João Vítor Aguiar Vieira Caetano
Co-Supervisors:	Doctor Paulo António Alves Ribeirinha
Member of the Committee:	Doctor Luísa Manuela Madureira Andrade

Sintra, June 2022

“Mudam-se os tempos, mudam-se as vontades,

Muda-se o ser, muda-se a confiança;

Todo o mundo é composto de mudança,

Tomando sempre novas qualidades.”

Luís Vaz de Camões

The use of trademarks or names of manufacturers in this dissertation is for accurate reporting and does not constitute an official endorsement, either expressed or implied, of such products or manufacturers by neither the Portuguese Air Force Academy nor the author.

Agradecimentos

A concretização desta dissertação não teria sido possível sem o apoio de todos aqueles que me acompanharam, direta ou indiretamente, durante não só o decorrer do projeto, como no longo percurso que me trouxe até aqui. A todos deixo uma franca palavra de agradecimento, de forma especial aos seguintes.

Ao Major Engenheiro Aeronáutico João Caetano, que desde o primeiro dia me disse que este projeto seria um grande desafio. Sem a sua coragem este tema não teria avançado e nada disto seria possível, agradeço por nunca desistir do nosso projeto mesmo quando parecia não haver outra alternativa. Pela incansável procura do melhor tema para cada aluno, mesmo tendo que atravessar muitas barreiras pelo caminho. Um grande obrigado pela disponibilidade, conselhos, rigor científico, e por manter sempre os níveis de motivação em alta.

Ao doutor Paulo Ribeirinha, sem o qual esta dissertação seria uma página em branco. Agradeço pela paciência e pela confiança em mim depositada. Confiança que sempre me permitiu ter uma palavra a dizer acerca do rumo do projeto, apesar das minhas escassas qualificações, bem como liberdade para aprender com os meus próprios erros. Por nos mostrar o melhor caminho quando nada parecia resolver os problemas, pelo *know-how* e exigência, o meu sincero agradecimento.

Ao ADAI, na pessoa da professora Ana Miranda, pelos valiosos dados recolhidos em incêndios florestais, sem os quais esta dissertação perderia muito do seu valor. A vossa disponibilidade espelha o que deve ser o espírito de partilha da comunidade científica, não deixando a distância impedir a boa transmissão de conhecimento.

A todos os membros do LEPABE, em especial ao Carlos, Yulia, Cátia, Sofia, Tânia, Luís, Paranjeet e Tiago Araújo, pela forma excecional como me receberam, pelos valiosos conselhos e por toda a ajuda que prontamente disponibilizaram sempre que precisei ao longo destes meses. Todos vocês tiveram um contributo nesta tese.

Aos meus colegas de laboratório e amigos Tiago Santos, Raquel, Ricardo e Francisco, por me fazerem sentir em casa num meio que não era o meu, por me ensinarem o que está nos livros e o que não está, e por me terem acompanhado de perto nesta jornada. Sem vocês a minha passagem pela FEUP não teria metade do valor que teve.

Ao meu curso, àqueles que me levantam nos piores momentos e me enaltecem nos melhores, um grande obrigado a todos os KAISERS. Juntos passámos momentos que nos unirão para a vida, independentemente do desígnio de cada um. Esta etapa simboliza mais um passo rumo à segunda asa. Juntos a conquistaremos. Queria deixar também um agradecimento especial às minhas "Marias" João Almeida, Tomás Garcia, Bruno Santos e Mauro Santos, pela amizade e paciência, quer nos momentos de descontração como nos longos serões de trabalho, a vossa ajuda foi preciosa.

A toda a minha família pelo apoio, afeto, suporte e estabilidade, em especial à Minita, ao José, e à minha avó Tina. Muito obrigado por serem sempre o meu pilar, nunca estaria onde estou sem vocês.

Por fim, deixo um agradecimento muito especial à Rita Costa por muitos anos de compreensão, preocupação, amor e carinho, pelo apoio nos bons e nos maus momentos durante estes meses de trabalho, e pelas excelentes revisões gramaticais. O teu orgulho alimenta a minha vontade de ir mais longe, em tudo o que faço.

Abstract

Green regulations and environmental concerns push the vehicle industry to study, invest and develop carbon-neutral systems. Hydrogen fuel cells offer a zero-emission solution to feed an electrical engine while demonstrating higher specific energy than traditional lithium-ion batteries, which translates to increased endurance.

Air contaminations found in areas of operation of the Portuguese Air Force cause significant degradation in the aircraft that operate in these conditions. Moreover, durability is one of the extensive challenges in proton exchange membrane fuel cells, as chemical and physical degradation phenomena hinder the system's performance over time. This thesis aims to study the response of fuel cells to contaminations mimicking those found in military aircraft operating conditions.

After system optimisation and baseline testing, NaCl, CO, and NO contaminations were admitted into the fuel cell cathode. Firstly in values similar to those found in wildfire and maritime environments, and then in more significant concentrations. Contamination periods vary from 30 to 60 hours. The NaCl and NO tests revealed that these contaminations have a minimal reversible effect on performance for the periods, conditions, and concentrations studied.

CO tests determined some irreversible losses, namely a 17 % drop in Electrochemical Surface Area, suggesting significant blockage of catalytic sites. Hence, prolonged wildfire operation is unadvised. Anode CO contamination was also conducted for comparison and validity purposes, revealing high monoxide adsorption in the anode catalyst layer. Lastly, *ex-situ* analyses were undertaken to support the performance results.

Keywords: Proton Exchange Membrane Fuel Cell (PEMFC); Degradation; Membrane Poisoning; Impedance Spectroscopy; Electrochemical Surface Area (ECSA).

Resumo

A crescente consciencialização ecológica tem levado a indústria dos transportes a estudar, investir e desenvolver sistemas neutros em carbono. Células de combustível oferecem uma solução de emissões zero para alimentar um motor elétrico, ao mesmo tempo que demonstram uma energia específica mais elevada do que as baterias tradicionais de lítio, o que se traduz num aumento da autonomia.

Contaminações atmosféricas encontradas nas áreas de operação da Força Aérea Portuguesa causam uma degradação significativa nas aeronaves que operam nestas condições. Esta tese visa estudar a resposta das células de combustível a contaminações semelhantes às encontradas nas condições de operação de aeronaves militares.

Após otimização do sistema e testes de base, foram admitidas contaminações de NaCl, CO, e NO no cátodo da célula de combustível. Inicialmente em valores semelhantes aos encontrados em ambientes marítimos e de incêndios florestais, progredindo depois para concentrações mais significativas. Os períodos de contaminação variam de 30 a 60 horas. Os testes NaCl e NO revelaram que estas contaminações têm um efeito reversível mínimo no desempenho durante os períodos, condições, e concentrações estudadas.

Os testes de CO determinaram algumas perdas irreversíveis, nomeadamente uma queda de 17 % na ECSA, sugerindo um bloqueio significativo dos locais catalíticos. Por conseguinte, a operação prolongada acima de incêndios florestais não é recomendada. Contaminações de CO no ânodo foram conduzidas para efeitos de comparação e validade, revelando uma elevada adsorção de monóxido na camada catalítica do ânodo. Finalmente, foram realizadas análises *ex-situ* para validar os resultados.

Palavras-Chave: Proton Exchange Membrane Fuel Cell (PEMFC); Degradação; Contaminação de Membrana; Espetroscopia de Impedância; Área de Superfície Eletroquímica (ECSA).

Table of Contents

AGRADECIMENTOS I
ABSTRACT III
RESUMO IV
TABLE OF CONTENTS V
LIST OF FIGURES VII
LIST OF TABLES IX
LIST OF SYMBOLS XII

CHAPTER 1 INTRODUCTION 14

1.1 Background and Motivation 2
1.2 Objectives 4
1.3 Dissertation Outline 5

CHAPTER 2 LITERATURE REVIEW 7

2.1 Chemical and Energetic Principles 8
2.1.1 Energy production and efficiency 10
2.1.2 Voltage Loss 11
2.1.3 Hydrogen Based Energy System 13
2.2 Technology Overview 17
2.2.1. Main types of fuel cells 17
2.2.2 Hybrid Systems 21
2.2.3 H_2/O_2 vs H_2/Air 22
2.2.4. Comparative study and application for military UAS 23
2.3 PEMFC as Aircraft Power Supply 24
2.3.1 Required Hardware 25
2.3.2 Weight Management 25
2.4 Fuel Cell Degradation 27

CHAPTER 3 MATERIALS AND METHODS 29

3.1 Test Bench and Cell specification 30

3.2 Contamination Tests *32*
3.3 Characterisation Techniques and Procedures *34*
3.3.1 In-situ Electrochemical Techniques 34
3.3.2 Ex-Situ Physical Techniques 35
3.3.3 Test Protocol and Optimal Operating Conditions 36
CHAPTER 4 RESULTS AND DISCUSSION 41
4.1 Fuel Cell Performance Assessment *42*
4.2 Maritime Operation - NaCl Contamination *42*
4.3 Wildfire Operation - CO and NO Contamination *46*
4.3.1 CO Cathode Contamination 46
4.3.2 NO Contamination 51
4.4 Ex-situ Test Analysis *55*
4.4.1 SEM 55
4.4.2 TPD 58
4.1.3 ICP-MS 60
4.5 Set Comparation *60*
CHAPTER 5 CONCLUSIONS AND FUTURE WORK 65
5.1 Conclusion *66*
5.2 Future Work *68*
BIBLIOGRAPHY 69
APPENDIXES 74
ANEXXES 82

List of Figures

Figure 1- Grove's experiment; a)- The electrolysis of water, (b)- Hydrogen and oxygen recombining, creating a small current (Larminie & Dicks, 2003)..... 8

Figure 2- E^0 dependence on temperature (Rayment & Sherwin, 2003). 11

Figure 3- Plot for voltage vs. current density (known as polarisation curve) as per Rayment and Sherwin, (2003)..... 12

Figure 4- Hydrogen square, four corners model by Dawood *et al .*, (2020) 13

Figure 5- Origin of commercially produced hydrogen, in 2019, as per Kayfeci *et al.*, (2019) 14

Figure 6- Details of a PEMFC, as demonstrated in Pan *et al* . (2019) 18

Figure 7- Reconstructed version of the AFC used in Apollo missions (Burke, 2003). 19

Figure 8- Theoretical energy densities, adapted from (Dyer, 2002) 21

Figure 9- Chart summarizing the applications, main advantages. operating temperatures and efficiencies of fuel cells of different types, adapted from (EG&G Services, 2000; Larminie & Dicks, 2003; Rayment & Sherwin, 2003) 23

Figure 10- Fuel cell system diagram in aircraft, as per Bradley *et al .*, (2007)..... 26

Figure 11- Test bench overview: 1- Zenium PRO potentiostat; 2-Additional control box; 3-PP241; 4- Flow and Pressure controller board; 5- Anode HPLC pump; 6- Cathode HPLC pump; 7- Scientific oven series 2000 for cell temperature control; 8- Water deposit..... 31

Figure 12- Open oven: 1- Oven control interface; 2- Anode Bubbler; 3- Cathode Bubbler; 4- Fuel cell 31

Figure 13- Contamination test protocol summary 39

Figure 14- Potential evolution with operation time, for a current density of 0.4 A cm^{-2}, after 20 h activation. 42

Figure 15- NaCl contamination: Potential evolution with operation time, for specific 0.4 A cm^{-2} A current density, with increasing NaCl contamination injection in the cathode, (concentrations of 0,1 mg L^{-1}, 10 mg L^{-1}, 10 g L^{-1} were added to the air inlet side bubbler). 43

Figure 16- Descending Polarisation curve in BoL and EoT salt contamination characterisation sets 1 A/cm^2..... 44

Figure 17- EIS Nyquist plots performed at the BoL and EoT characterisation, being performed at A) 0.02 A cm^{-2}, B) 0.2 A cm^{-2}, C) 0.4 A cm^{-2} and, E) 0.6 A cm^{-2}..... 45

Figure 18- Cyclic voltammetry plots performed for NaCl contamination experiments, for the BoL and EoT. Cyclic voltammetry was performed at 20 mV s^{-1} scan, with 200 mL of H_2 and N_2 feed, for the anode and cathode, respectively. 45

Figure 19- First CO contamination: Potential evolution with operation time, for specific 0.4 A cm^{-2} A current density, with increasing CO contamination injection in the cathode, (concentrations of 13 ppm, 50 ppm and 75 ppm of CO were added to the PEMFC air inlet). 47

Figure 20- Second CO contamination: Potential evolution with operation time, for specific 0.4 A cm^{-2} current density, with increasing CO contamination injection in the cathode (concentrations of 50 ppm and 75 ppm were added to PEMFC the air inlet). 48
Figure 21- Second MEA: Descending Polarisation curve in BoL and EoT characterisation sets. 49
Figure 22- Second MEA: EIS Nyquist plots performed at the BoL and EoT characterisation, being performed at A) 0.02 A cm^{-2} and 50 mA amplitude, B) 0.2 A cm^{-2} and 200 mA amplitude, C) 0.4 A cm^{-2} and 500 mA amplitude, E) 0.6 A cm^{-2} and 1 A amplitude. 50
Figure 23- Cyclic voltammetry plots performed for CO contaminations experiments, for the BoL and EoT. Cyclic voltammetry performed at 20 mV s^{-1} scan, with 200 mL of H_2 and N_2 feed, for the anode and cathode, respectively. 50
Figure 24- NO contamination: Potential evolution with operation time, for fixed 0.4 A cm^{-2} current density, with increasing NO injection in the cathode (concentrations of 2 ppm and 20 ppm of NO were added to the air inlet stream). 52
Figure 25- NO test: polarisation curve before and after NO contamination at the air inlet stream, performed at 1 A cm^{-2} feeding gases. 53
Figure 26- NO contamination: EIS Nyquist plots performed at the BoL and EoT characterisation, being performed at A) 0.02 A cm^{-2} and 50 mA amplitude, B) 0.2 A cm^{-2} and 200 mA amplitude, C) 0.4 A cm^{-2} and 500 mA amplitude, E) 0.6 A cm^{-2} and 1 A amplitude 53
Figure 27- Cyclic voltammetry plots performed for NO contamination experiments, for the BoL and EoT. Cyclic voltammetry performed at 20 mV s^{-1} scan, with 200 mL of H_2 and N_2 feed, for the anode and cathode, respectively. 54
Figure 28- A, B, C, and D show different points of analysis of possible salt degradations in the cathode gas diffusion layer (GDL) in MEA1. 55
Figure 29- Anode GDL of the CO contaminated membrane. 56
Figure 30- Cross section SEM images. Membrane, CL and GDL Thickness displayed. 340x to 780x: A) Pristine Sample. B) NaCl sample. C) Cathode CO sample 380x. D) Cathode CO sample 780x. 57
Figure 31- TPD sample test profiles referring to pristine and CO contaminations in the cathode and anode. In the caption, "Cathode/ anode contamination" and "pristine" refer to the tests elaborated on each membrane analysed in the TPD. "MEA" indications mean the whole membrane was analysed, and "GDL" indication means only the cathode side GDL composed the sample. The samples were heated at 10 °/min.. 58
Figure 32- - MS results regarding CO-contaminated samples show small peaks in temperatures similar to the obtained TPD results. 59
Figure 33- MS results regarding the pristine sample 60
Figure 34- Comparison of the performance evolution of different test sets: A) Galvanostat mode B) Potentiostat mode 62
Figure 35- Comparison of the ECSA variation during all test sets 63

List of Tables

TABLE 1- WEIGHT DISTRIBUTION OF THE DEMONSTRATORS, PRESENTED IN THE FORMAT: COMPONENT WEIGHT [% OF TOGW] (BRADLEY *ET AL* ., 2007; SWIDER-LYONS *ET AL* ., 2011) 26
TABLE 2- CONTAMINATIONS IN LITERATURE SUMMARY 28
TABLE 3- MEMBRANE SPECIFICATIONS SUMMARY 32
TABLE 4- OPTIMIZED OPERATING CONDITIONS FOR CONTAMINATION TESTS. 37
TABLE 5- MEASURED MEMBRANE THICKNESS ACROSS SAMPLES. 57

Abbreviations

AC	Alternating Current
AFARC	Air Force Academy Research Centre
AFC	Alkaline Fuel Cell
BOL	Beginning of Life
CHP	Combined Heat and Power
CL	Catalyst Layer
CV	Cyclic Voltammetry
DC	Direct Current
DL	Diffusion Layer
DMFC	Direct Methanol Fuel Cell
EIS	Electrochemical Impedance Spectroscopy
EMF	Reversible Open Circuit Voltage for A Hydrogen Fuel Cell.
EOL	End of Life
EOT	End of Test
EU	European Union
HEV	Hybrid Electric Vehicle
HOR	Hydrogen Oxidation Reaction

ICP	Inductively Coupled Plasma
MCFC	Molten Carbonate (Electrolyte) Fuel Cell
MEA	Membrane Electrode Assembly
MEA	Membrane Electrode Assembly
MS	Mass Spectroscopy
OCV	Open Circuit Voltage
ORR	Oxygen Reduction Reaction
PAF	Portuguese Air Force
PAFC	Phosphoric Acid (Electrolyte) Fuel Cell
PEMFC	Proton Exchange Membrane Fuel Cell
PSI	Pounds Per Square Inch
SEM	Scanning Electron Microscopy
SOFC	Solid Oxide Fuel Cell
STP	Standard Temperature and Pressure (25ºc and 1 bar)
TPD	Temperature Programmed Desorption
UAS	Unmanned Aerial Systems
UAV	Unmanned Aircraft Vehicle

List of Symbols

ΔG^0	Change in Gibbs free energy at standard temperature and pressure, and with pure reactants
qPt	Charge Density ($\mu C\ cm^{-2}_{electrode}$)
Γ	Charge required to reduce a monolayer of protons ($210\ \mu C\ cm^{-2}_{Pt}$)
I	Current (A)
i	Current density ($A \cdot cm^{-2}$)
η	Efficiency
E	EMF or open circuit voltage (V)
H	Enthalpy (J)
$(\Delta_f H^\circ)_X$	Enthalpy of formation per mole of substance X ($J\ mol^{-1}$)
F	Faraday constant, the charge on one mole of electrons (96,485 *C*)
ΔG°_f	Gibbs free energy of formation per mole ($J\ mol^{-1}$)
$(\Delta_f G^\circ)_X$	Gibbs free energy of formation per mole of substance X
Z	Impedance (Ohm)
η_c	Isentropic efficiency (of compressor or turbine)
m	Mass *(kg)*
R	Molar or 'universal' gas constant $8.314\ (J\ K^{-1}\ mol^{-1})$also electrical resistance (Ω)
L	Pt loading in the electrode ($g_{Pt}\ cm^{-2}_{electrode}$)

λ	Stoichiometric ratio
t	Time (s)
V	Voltage (V)

Chapter 1 Introduction

This chapter establishes the context of the thesis. Starting with a brief historical overview, it then presents the main motivations and objectives of the study, as well as the reasons that make it significant. It finalizes with a brief description of the structure of the dissertation.

1.1 Background and Motivation

For more than a century, since the birth of heavier-than-air aviation, researchers, engineers, technicians, and pilots, such as Portuguese pioneers Sacadura Cabral and Gago Coutinho, have worked on taking aviation further, higher and faster, making it safer, more efficient and, more recently, "greener". In this sense, the various systems that form an air platform have undertaken considerable improvements recognition. An evolution that started by the control of a low duration flight, which attended the needs of two world wars, led to today's multidisciplinary subject that allows transcontinental transport, search and rescue missions, and worldwide maritime and terrestrial surveillance.

Recently, unmanned aviation has witnessed relevant technological advances and widespread civil and military use, thanks to the proven advantages that it offers in various missions, mainly those described as *dull*, *dirty*, and *dangerous*, over manned systems (Franco *et al* ., 2019).

In Portugal, for the last decade, the inevitable military adherence to unmanned aerial systems (UAS) were introduced in 2006 by the Air Force Academy Research Centre (AFARC). Based in Academic research, AFARC has developed successful work fulfilling the operational needs of the Armed Forces (AF) regarding unmanned flight, mainly during the PITVANT programme (Oliveira, 2014).

The Portuguese Air Force (PAF) defined as part of its strategic vision, the creation of a national unmanned air capacity, specifically, the integration and use of Class II and III UAS in surveillance, reconnaissance and patrol missions (Força Aérea Portuguesa, 2019). One of the requirements is a multipurpose and multidisciplinary aircraft with a minimum flight endurance of 9 hours. Missions such as maritime and firefighting intelligence, surveillance and reconnaissance (ISR) missions clearly demand a flight range and endurance that unmanned systems in the PAF do not possess at the present moment.

Consequently, research projects should point to achieve performance standards that enable UAS to accomplish these missions. Undoubtedly, one of the most critical areas for enhancing flight endurance and range is related to the propulsion system. The main technological challenge

that motivates this thesis is extending the endurance of the tactical, low weight Unmanned Aerial Vehicles, while making their operation more environmentally friendly.

In July of 2020, the Portuguese Minister Council approved the National Energy and Climate Plane 2030 (*Plano Nacional Energia e Clima 2030* -- PNEC 2030). This programme, aligned with the long-term strategy of the European Commission of aiming for a climate-neutral EU by 2050, sets concrete climatic and energetic goals for the year 2030, among them[1]:

a) Reducing greenhouse gas emissions by 45 % to 55 %, concerning the registered emissions of 2005.

b) Reaching an overall energy efficiency of 32,5%.

As a result of these determinations, efforts have been made to reduce the carbon footprint of the transport sector, which is mostly based on internal combustion engines, and according to Gröger *et al* . (2015), is responsible for approximately 23% of the worldwide CO_2 emissions. The Carnot cycle efficiency in internal combustion engines is *ca.* 40 %, while an electric motor is capable of reaching values between 90 and 100 % (Pan *et al* ., 2019). It is then clear that electric propulsion provides a more efficient solution, with reduced carbon footprint, and lower cost.

However, lithium battery technology, the most common application for tactical UAS , provides lower specific power and specific energy (Lapeña-Rey *et al* ., 2017), when compared to fossil fuel counterparts. On the other hand, hydrogen fuel cells offer rapid refuelling, higher specific power and specific energy. The thermodynamic efficiency of hydrogen fuel cells is 83 %, which is twice the efficiency of internal combustion engines. Besides, fuel cells offer low noise, low infrared signature and, since the only product of fuel cell propulsion systems is water, zero emissions (Pan *et al* ., 2019). There is yet no record of hydrogen propulsion or any electrochemical hydrogen powered energy source in any of the PAF aircraft or energy production.

[1] Source: *(Presidência Do Conselho De Ministros,* 2020)

1.2 Objectives

The main objective of this work is to test the concept of a zero-emission hydrogen fuel cell system, as the main source of energy for an electric propulsion tactical low weight fixed wing Class I [2] UAS, adapted for the Portuguese Air Force's operational needs. To achieve that, this work aims to test generic fuel cells in environments mirroring the ones faced by UAS in real areas of operation, as per below.

Furthermore, a set of secondary objectives must be attained throughout the thesis:

- Overview of the available technology and current state of the technology.
- Comparison and selection of the possible fuel cells stacks to be used by AFARC.
- Performance analysis and characterisation of the single cell used in the practical study.
- Contamination tests simulating environments 500 ft above the ocean and 500 ft above wildfires.
- Analysis of results and impact on implementation of hydrogen fuel cells in a PAF designed UAS.

[2] NATO Classification: Class I: <150 kg; Class II: 150-600 kg; Class III: >600 kg

1.3 Dissertation Outline

The present document is comprised of six chapters. Following the present section, chapter two presents state of the art, representing the thesis's theoretical pillars. Concepts are presented which detail chemical and energetic principles, and the description of processes later used to compare and better understand the fuel cell systems.

The dissertation progresses in chapter two into the systemic analysis of the different available systems, their performance and applicability to the scope of the thesis is studied and analysed, and among them is selected the most suitable system for the PAF mission and for the experiments of the study.

In chapter three, the groundwork for the practical study is described. The resources, equipment and testing systems are specified, and so are the techniques, approaches, and overall testing plan used.

Following the output of chapters two and three, the fourth chapter details the results obtained in the contamination tests. The performance of the degraded cell is analysed recurring to a number of testing methods, repeated for all contaminations chosen. After the experiments, *ex-situ* techniques are used to assess the extent of the contaminations, and a comparison and discussion on the results obtained is done.

Lastly, the fifth chapter presents the conclusions of the thesis. It reflects on the work done, the difficulties, and recommendations for future studies.

INTENTIONALLY LEFT BLANK

Chapter 2 Literature Review

This chapter provides the theoretical concepts regarding the practical study that it preludes. It starts with a description of the principles of a fuel cell and a hydrogen-based system. Then, an overview and analysis of the existing technology is made, presenting the chosen systems. Lastly, the requirements for aerial operation are presented and analysed.

2.1 Chemical and Energetic Principles

In 1839, Sir William Grove first demonstrated what would become the forerunner to the modern fuel cell. He did so using a reasonably simple experiment, depicted in Figure 1: Two platinum (Pt) electrodes connected through an external circuit and placed inside of two separately sealed containers filled with diluted sulphuric acid. When electric current passes through the electrodes results in the decomposition of water into oxygen and hydrogen. This process is called the water electrolysis, has it been previously discovered by Troostwijk and Deiman (de Levie, 1999).

But Grove proved that if an ammeter replaced the power supply, oxygen and hydrogen would recombine, forming water, and a small current would flow through the ammeter, he called it the "gas battery". This simple experiment is a demonstration of the basic principle of a fuel cell and can be summed up by the following expression:

$$O_2 + 2H_2 \rightarrow 2H_2O \qquad E^0 = 1.229\text{V} \quad [2.1]$$

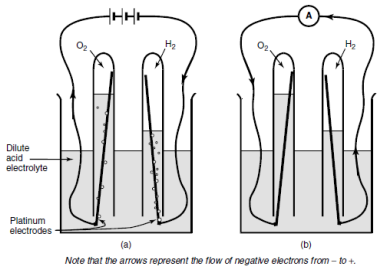

Figure 1- Grove's experiment; a)- The electrolysis of water, (b)- Hydrogen and oxygen recombining, creating a small current (Larminie & Dicks, 2003).

To understand this reaction, it is necessary to consider the half reactions taking place at each electrode. These reactions slightly vary for different types of fuel cells, as detailed in the next section. However, Grove's acid electrolyte fuel cell is the simplest and most common.

At the anode of an acid electrolyte fuel cell, hydrogen ionises, releasing H^+ ions (protons) and electrons.

$$2H_2 \rightarrow 4H^+ + 4e^- \quad [2.2]$$

At the cathode, oxygen reacts with the by-products of equation 2.2, forming water.

$$O_2 + 4e^- + 4H^+ \rightarrow 2H_2O \quad [2.3]$$

For reaction 2.3 to happen continuously, protons and electrons released at the anode must be made available at the cathode. Electrons pass through an electrical circuit that connects the anode and the cathode, creating current, and H^+ ions must be able to pass through the electrolyte. The diluted sulfuric acid, being a fluid in which H^+ ions move freely, serves this purpose in Grove's experiment.

Certain polymers, such as Nafion™ can also allow the transport of protons. The high proton conductivity and mechanical stability at temperatures of 313 K – 363 K under fully hydrated conditions, makes Nafion™, one of the most used in proton exchange membrane fuel cell (PEMFC). This type of fuel cell is detailed in section 2.2.1.1.

A significant advantage of fuel cells is that this system does not require recharging in the same way as batteries. Thus, theoretically, a fuel cell can produce useful electrical energy for as long as it is supplied with fuel, *e.g.,* in this case, a useful voltage range is directly dependent on the reaction rate of the fuel, which can be enhanced by using more active electro-catalysts, improving the proton conductivity of the electrolyte or reducing its thickness.

The electrode active area is a vital issue in the fuel cell performance. Modern electrodes have a microstructure that gives them surface areas that can be hundreds or thousands of times their straightforward 'length × width' (Larminie & Dicks, 2003). Likewise, the design of the electrode must maximise the area of contact through porous electrodes, optimise the penetration and minimise the distance between both electrodes.

2.1.1 Energy production and efficiency

The energy produced by the electrochemical reactions described earlier (Eq. 2.2 and 2.3) can be calculated from the Gibbs free energy of the water formation ($\Delta_f G$) representing the energy available for external work. The value of $\Delta_f G$, for the specific case of PEM cells, depend on the reactants, temperatures and pressures, as given by the following expression:

$$\Delta_f G = \Delta_f G^o - RT_{fc} \ln\left[\frac{pH_2 P_{O_2}^{\frac{1}{2}}}{PH_2O}\right] \quad [2.4]$$

where R is the universal constant for ideal gases, P_{H_2} is the hydrogen partial pressure, P_{O_2} is the oxygen partial pressure, P_{H_2O} the water vapour partial pressure, T_{fc} is the operating temperature and ΔG_f^o the Gibbs free energy at standard conditions (Kunusch *et al* ., 2012).

Some authors define efficiency as the ratio between the output and input energy. In this specific case, input energy is the enthalpy of water formation. Considering that two electrons are involved in the reaction, the maximum theoretical efficiency of a PEM fuel cell at 25ºC can be calculated as such:

$$\eta_{max} = \frac{-\Delta_f G}{-\Delta H} = \frac{\frac{-\Delta_f G}{2F}}{\frac{-\Delta H}{2F}} = \frac{1.229}{1.482} = 0.83 \quad [2.5]$$

where $-\Delta G_f^o /2F$ = 1.229 V is the theoretical reversible voltage of an open circuit for a hydrogen cell, or E^o, and $-\Delta H/2F$ = 1.482 V is the value of the thermoneutral voltage (the resulting voltage if all the enthalpy of hydrogen is converted into electric energy).

In such manner, as stated by Kunusch *et al* ., (2012), the efficiency of the hydrogen fuel cell can be obtained at any condition simply from the voltage at its output terminals (*Vfc*), using:

$$\eta = \frac{V_{fc}}{1.482} \quad [2.6]$$

2.1.2 Voltage Loss

The E^o for an open circuit of 1.229 V is never truly attained. Therefore, it is essential to understand the systems losses, find models and equations closer to real life, and find ways to minimise these losses. As seen before, the temperature directly affects the ΔG_f of the fuel cell, and, as can be seen in Figure 2, low-temperature fuel cells have a higher theoretical E^o than high-temperature fuel cells (Kunusch *et al*., 2012).

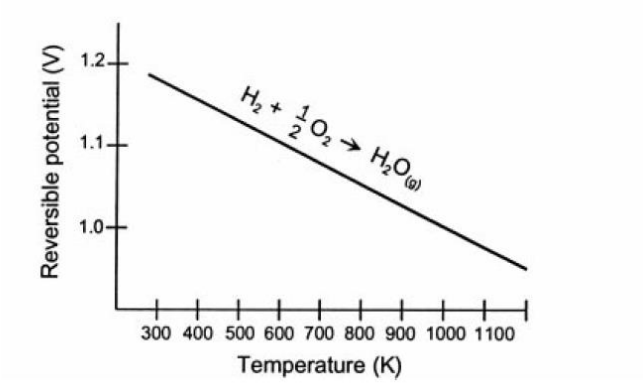

Figure 2- E^0 dependence on temperature (Rayment & Sherwin, 2003).

These losses can be broken up into four categories: activation losses, fuel crossover losses, mass transport losses, and ohmic losses.

- Activation energy must be overcame to force the reaction to completion. Activation losses are associated with the initiation of the chemical process. This loss is preeminent at low current densities in low-temperature cells.
- Fuel crossover loss corresponds to the energy that is dissipated through the proton transfer. Fuel leakage in the electrode is the main cause, although electrons also cross the slightly conductive electrode. Different modifications of the Tafel equation can model both crossover and activation losses. These losses can affect all the operation voltage range.
- Ohmic losses are expected across any electrical device and are the most significant source of loss in low and high-temperature fuel cells. This happens, more significantly in the electrolyte, due to resistance to protons flow and in the electric contact between the cell components, due to resistance to electron flow. It is directly dependent on current density

and area-specific resistance. High conductive materials, thin electrodes and hot-pressing attenuate these losses.

- Mass transport losses reflect changes in the local concentration of reactants. When the cell consumes fuel or oxygen faster than it can be supplied, the partial pressures of O_2 and H_2 drop; this loss is only prevalent at high current densities. The Nernst equation can determine the change of voltage.

Combining these four types of losses results in an approximation of the actual operational graph and equation, (Rayment & Sherwin, 2003) as follows:

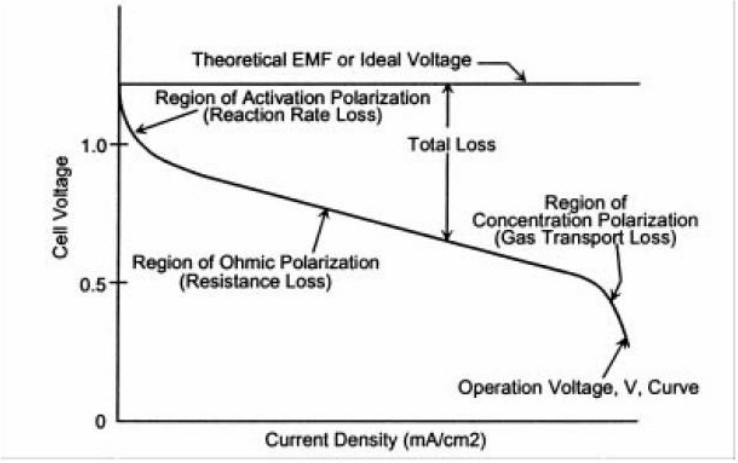

Figure 3- Plot for voltage vs. current density (known as polarisation curve) as per Rayment and Sherwin, (2003)

2.1.3 Hydrogen Based Energy System

Dawood *et al* . (2020) identified that the hydrogen energy system comprises four main stages, interconnected and interdependent. The author describes them as corners of the same square, represented in Figure 4: production, storage, safety and utilisation. With utilisation already covered, this section will cover the three remaining stages, namely some of the several production technologies and storage requirements of hydrogen systems.

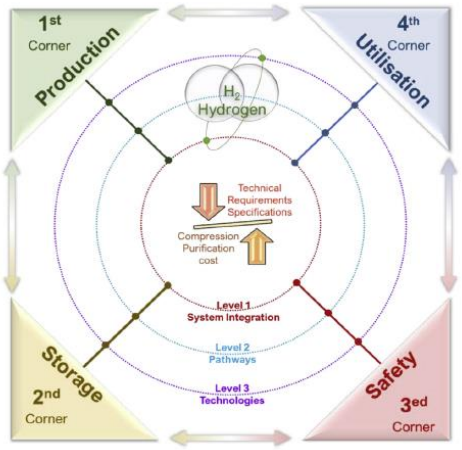

Figure 4- Hydrogen square, four corners model by Dawood et al ., (2020)

This chapter realised that vehicles employing a PEMFC running on hydrogen could be termed *zero-emission*, as its only by-product is water. Notwithstanding, hydrogen, being a highly reactive element, is only found in nature combined with other elements, so the method of hydrogen production determines the cleanness of the energy source.

Data from 2019, by Kayfeci *et al.* (2019), shows that most of the hydrogen that is commercially produced still relies mainly on carbon emission-based methods; Figure 5 illustrates the origin of the H_2 made commercially today. Despite that, various clean ways are practicable on a small scale, and in the long term, they will be ready to be used for commercial purposes.

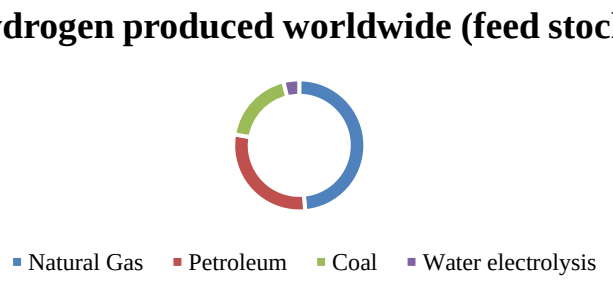

Figure 5- Origin of commercially produced hydrogen, in 2019, as per Kayfeci et al., (2019)

2.1.3.1 Fossil Fuels

The most common and inexpensive methods to produce hydrogen are also the most harmful to the environment. The catalytic steam reforming of natural gas, partial oxidation of petroleum, steam iron treatment, and coal gasification are the most common processes for hydrogen production (Kayfeci *et al* ., 2019). The fossil fuels, hydrocarbons, and steam are heated, combined in a reactor, then are broken down and recombined, into H_2, CO, and CO_2, generally.

The gasification of coal is the oldest production method. The coal is heated to 900 ºC, where, in the presence of steam and/or oxygen, it gasifies, generally promoted by a nickel catalyst. The high temperatures required, the production of CO and CO_2 and the operational issues (*e.g*. clogging of reactors due to production of tars) make this process obsolete (Holladay *et al* ., 2009).

Methane steam reforming is the most used technology nowadays. The principle is similar to coal gasification, in this case, methane and steam react in catalytic reactors to produce H_2 and CO (Eq. 2.7) Liquid petroleum gases, methanol, gasoline and ethanol can also be reformed using a similar process.

$$CH_4(g) + H_2O + \text{heat} \rightarrow CO + 3H_2 - 206\ \text{kJ mol}^{-1} \quad [2.7]$$

2.1.3.2 Water splitting

About 11.1% of water is hydrogen, being this the most abundant hydrogen source on the planet. Burning hydrogen produces water, so transforming this water into hydrogen closes an entirely renewable energy cycle. Hydrogen can be produced from water by electrolysis, thermal decomposition, or thermochemical methods.

Among these processes, electrolysis is the most efficient (Rossmeisl *et al* ., 2005) – described in chapter 2.1.1. – and it is an endothermic reaction, attaining efficiencies between 56-73 %. Similar to fuel cells, electrolysers can be alkaline, solid oxide, or proton exchange membranes. The alkaline electrolysers are the most mature technology, with low capital cost. Solid oxide electrolysers are the most efficient, and PEM electrolysers present highest current densities (Lee *et al* ., 2020).

Thermolysis is the process where water is heated to a temperature of *ca*. 2500 ºC, where the water molecules split into hydrogen and oxygen. The high temperature, pressure and corrosive environment require new materials, yet its high efficiencies can make it commercially viable (Holladay *et al* ., 2009).

2.1.3.3 Biomass and Biological

Biomass is pointed out as the best near term renewable alternative to fossil fuels. Fuels can be produced from biomass by gasification and pyrolysis.

Like fossil fuels, biomass is heated in the gasification process, transforming into a mixture of H_2, CO, and CH_4. The CO_2 released is considered "neutral", as it does not increase the CO_2 concentration in the atmosphere. This is a very mature and commercially used technique but can only be used on a large scale. Pyrolysis is the first step of a gasification process, and consists on the thermal decomposition of organic material, that allows the production of liquid fuels, such as bio-oils (Tanksale *et al* ., 2010).

Biological hydrogen is obtained from organic processes that use bacteria or algae. The main biological processes for bio-hydrogen production are photolytic hydrogen production using green

algae or cyanobacteria (also known as direct photolysis), dark-fermentative hydrogen production and photo-fermentative processes.

Some organisms use excess solar energy to produce hydrogen by the direct photolysis of water, using a process similar to photosynthesis. According to Ni *et al* ., (2006), researchers have been trying to reengineer microalgae to enhance the H_2 production and reduce photosynthesis to a survivability minimum. However, managing such a process for H_2 production is still unclear, and this method presents a very low production rate.

Another method is dark fermentation which involves the oxidation of substrate by bacteria under anaerobic conditions. It has high conversion speeds, however, it presents low conversion efficiency of the substrate (Kayfeci *et al* ., 2019). Many other processes, such as waste gas team recovery, microbial electrolysis cells, are also being studied.

In terms of production, one concludes that fossil fuel technologies are the most developed and by far the most profitable. In terms of low emission technology, the most promising process in the near term is electrolysis coupled with renewable energy. Electrolysis proves to be competitive in small scale production (Holladay *et al* ., 2009).

2.1.3.4 Safety and storage

Concerning safety, hydrogen is considered to be relatively safer than other fuels, as it is non-toxic and dissipates rapidly when released. The primary concern is that an undetected extended leak in a confined space will eventually ignite and cause an explosion, as its ignition energy is low (approximately 1/10 of the ignite energy of gasoline) (Dawood *et al* ., 2020; Weiner, 2014).

Regarding the storage units, as hydrogen has poor energy density by volume compared to hydrocarbons, it requires a larger tank to store; still, as the energy density by weight is high, the mass of the tank is smaller when compared to hydrocarbon solutions (He *et al* ., 2016). The gravimetric capacity using current tanks, is *ca.* 1.5 kWh kg^{-1} while the volumetric capacity is *ca.* 1.0 kWh L^{-1}, having an ultimate goal of 2.2 kWh kg^{-1} and 1.7 kWh L^{-1}, respectively (Abe *et al* ., (2019)).

2.2 Technology Overview

In this sub-section, the different types of existing cells and the most recent and relevant applications are thoroughly analysed to have an insightful outlook on the point of development of these technologies. These technologies are then compared, and an assessment is made about which is more suitable for a tactical low weight Class I UAS.

2.2.1. Main types of fuel cells

2.2.1.1. Proton exchange membrane Fuel Cells (PEMFC)

The conventional PEMFC consists of three main components: an anode, a proton exchange membrane (PEM), and a cathode. Anode and cathode are placed in contact on opposite sides of the PEM. Hydrogen oxidation occurs at the anode while oxygen reduction at the cathode. These reactions generate an electric potential difference between the electrodes (Pt-based) that can then be used to produce work. The entire reaction occurs if the electrolyte allows proton transport and isolates electrically both electrodes. (Kunusch *et al* ., 2012). These details are summarized in Figure 6.

The cells are connected in series to produce useful voltage, forming a stack. This is achieved using bipolar plates, that makes electrical connections between the cathode of one cell and the anode of the next cell, and, at the same time, the bipolar plate serves as means of feeding oxygen to the cathode and fuel gas to the anode.

Furthermore, electrodes in the PEMFC are composed of a gas diffusion layer (GDL) and a catalyst layer (CL). The GDL, usually a carbon paper or cloth with thickness between 0.2 to 0.5 mm, that diffuses the gas into the catalyst and creates an electrical connection between the bipolar plate and the catalyst. The CLs are usually made of Pt supported on carbon black mixed with an ionomer, resulting in the formation of triple-phase boundaries (TPBs) for electrochemical reactions (Pan *et al* ., 2019). Platinum (Pt) or palladium-based catalysts are pointed out as the best catalyst for both the hydrogen oxidation reaction (HOR) occurring at the anode and the oxygen reduction reaction (ORR) at the cathode, being one of the most expensive and components of the cell (Holton & Stevenson, 2013; Kunusch *et al*., 2012).

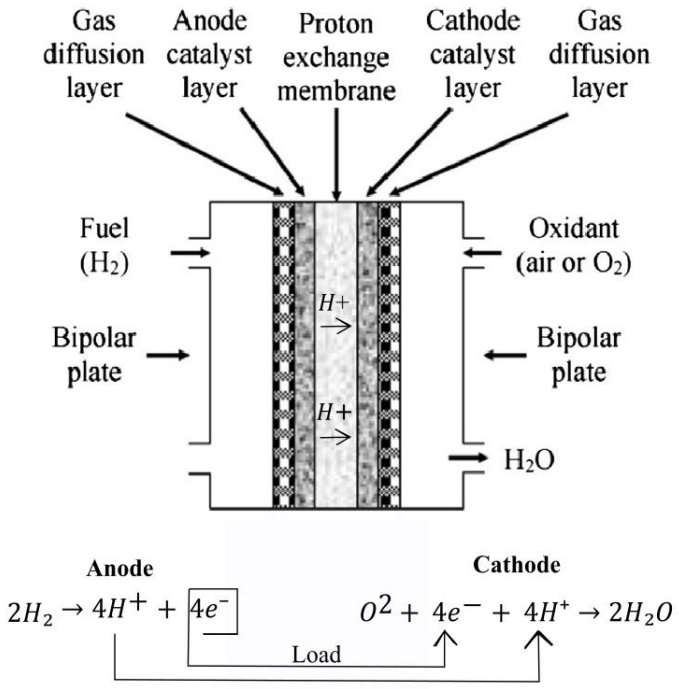

Figure 6- Details of a PEMFC, as demonstrated in Pan et al . (2019)

2.2.1.2. Other fuel cell types

Alkaline Fuel Cells (AFC) were demonstrated in the 1940s by Francis Thomas Bacon. Since 1960, NASA used AFCs (Figure 7) in the Apollo missions, due to their high thermal efficiency, *ca.* 70%. These cells operate at temperatures of 60-90ºC and follows the reactions described by Eq. 2.8 and 2.9 (Rayment & Sherwin, 2003).

The reaction at the anode is:

$$2H_2 + 4OH^- \rightarrow 4H_2O + 4e^- \quad [2.8]$$

At the cathode:

$$O_2 + 4e^- + 2H_2O \rightarrow 4OH^- \quad [2.9]$$

This type of fuel cell was tested in various applications and always resulted in some yet unsolved problems, such as cost, operability, durability and reliability. The main advantages they offer is that the activation overvoltage at the cathode is usually less than with an acid electrolyte fuel cell, and the possibility of less costly electrodes. However, high operating pressures and temperatures, and cryogenic storage systems make this technology unsuitable for small aircraft.

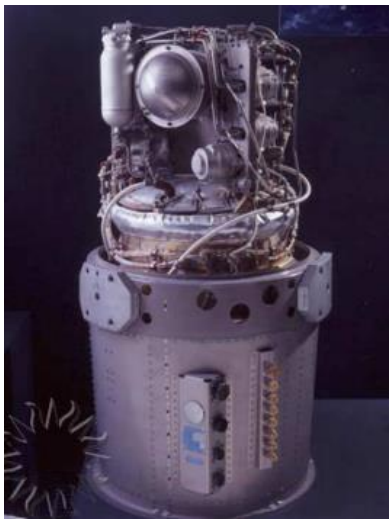

Figure 7- Reconstructed version of the AFC used in Apollo missions (Burke, 2003).

One of the most manufactured fuel cells of the modern industry, overcame only by PEMFC, is the Solid Oxide Fuel Cell (SOFC) (E4tech, 2021). These cells are a valid option for energy generation systems, by operating at very high temperatures (600ºC to 1000ºC), they attain

very high reaction rates without the need for expensive catalysts. The SOFC is a complete solid-state device that uses ceramic as an electrolyte. It can run on hydrogen or hydrocarbons, such as methanol or methane, and are very insensible to carbon monoxide or carbon dioxide. Ohmic losses are the most notable in this kind of cell (Choudhury *et al* ., 2013).

Although it is one of the most promising cells for distributed or centralised power generation, its operating temperature and configurations make this fuel cell impracticable for smaller applications such as hand-held devices and UASs.

Since storage, distribution and production of hydrogen are still facing implementation issues, some fuel cells offer fuel alternatives. The Direct Methanol Fuel Cells (DMFC), has similar physical structure of a PEMFC, yet the fuel used is a mixture of methanol and water, which react in the anode as expressed:

$$CH_3OH + \frac{3}{2}\,O_2 \rightarrow CO_2 + 2H_2O \qquad E^0 = 1.21V \quad [2.10]$$

According to some researchers, *e.g.* Kamarudin *et al* . (2009) and Rayment & Sherwin (2003) the DMFC are considered suitable power sources for portable energy applications. This is because DMFCs operate at low working temperatures due to the low methanol boiling temperature, this allows a very low size and weight, and can be designed for a longer cell lifetime. DMFCs can be a viable option for vehicle propulsion with further development; Goor *et al* . (2019) claims that these cells will be soon introduced to the market for small electric vehicles and portable electronics.

Energy density for methanol cells is substantially higher than that of pure hydrogen cells, *viz*. Figure 8. However, several barriers need to be surpassed before this happens, such as high crossover voltage loss and degradation rates, which cause the inability to get the full potential out of the anode and the cathode, and compromise the stability of the cell in the long term (Kamarudin *et al* ., 2009). Further types of fuel cells can be consulted in appendix B.

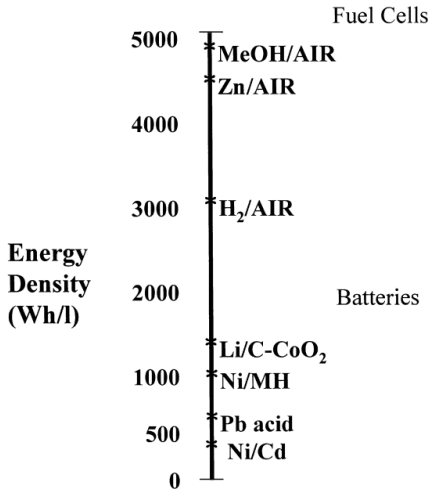

Figure 8- Theoretical energy densities, adapted from (Dyer, 2002)

2.2.2 Hybrid Systems

There are two main factors in the propulsion system that influence the performance of any aircraft, and that is specific power, associated with maximum speed, maximum take-off weight, and climbing rate; specific energy, mainly affects endurance.

Chen *et al* . (2009) reported that hydrogen solutions offer, at best, specific energy of 800–10,000 $Wh \cdot kg^{-1}$ and specific power up to 500 $W \cdot kg^{-1}$, while lithium-ion batteries provide around 75–200 $Wh \cdot kg^{-1}$ and 500–2000 $W \cdot kg^{-1}$ of specific energy and specific power, respectively. The specific energy of fuel cells can be up to three orders of magnitude superior to batteries, yet its specific power is actually lower. That means that a pure hydrogen-powered system can have superiority in terms of endurance over lithium solutions. However, its peak power would be lessened when compared to lithium-ion batteries.

This issue can be solved with a hybrid propulsion system, which could enable a UAS to perform a wider variety of missions, combining the high endurance of fuel cells and the peak power of lithium batteries. A hybrid electrical vehicle (HEV) is defined as a vehicle whose propulsion is supplied by two or more energy sources. Generally, Pan *et al* . (2019) sum up four advantages of relying on a hybrid system: i) downsizing each of the propulsion systems for the same amount of power generally means a weight reduction; ii) the existence of two independent systems allows for the fast demand of power variations to be corresponded; iii) it confers the

HEV with redundancy, continuing operation if one of the systems is malfunctioning; iv) hybrid systems possess the flexibility to deal with erratic availability of different energy sources.

Nishizawa *et al* . (2013) succeeded in testing a passive hybrid system consisting of fuel cell stacks, Lithium-ion battery packs, and two diodes. The diodes take the place of the DC/DC converter that is typically used to align fuel cell and battery voltages, directly linking the fuel cell and the battery. The system exhibited good efficiency and good response to dynamic load requests.

2.2.3 H_2/O_2 vs H_2/Air

A H_2/Air system is subject to factors external to the fuel cell, as it relies on oxygen from the surrounding air. Researchers have tested the impact of using a pure oxygen supply instead of air, and found that the advantages are more than simply ceasing to be dependent on the atmospheric conditions. Studies from Büchi *et al* . (2007) and (2005) conclude that pure oxygen systems have the following advantages over typical air systems: : i) higher power densities; ii) lower electrolyte cost, higher efficiency and iii) no possible poisoning due to poor ambient air quality.

Explicitly, at constant electrochemical cell efficiency (LHV), the specific power of the cell increases by up to 60%. This is due to the reduction of mass transport and ohmic losses, since the partial pressure of the O_2 in the anode increases five-fold if supplied directly in pure form, and because this system offers easier humidification of the cathode gas, respectively.

Moreover, as seen in section 2.1.4., hydrogen production in the recent future will primarily go through electrolysis or thermochemical pathways. In either case, pure oxygen will be a by-product of hydrogen production, reducing its energetic cost if a pure system is applied. In that way, power used in oxygen production was deduced as parasitic power in Büchi's work. The results showed a 20 % efficiency advantage for the pure oxygen system against the air system.

When oxygen production power was accounted for, it resulted in an efficiency drop of 3–5% for electrolytic oxygen and 10–12% for oxygen from liquid air distillation. The resulting efficiencies are still considerably higher than for current air-based systems. However, Büchi's work makes minimal reference to the influence of the additional weight of oxygen as a supplementary reactant.

2.2.4. Comparative study and application for military UAS

After analysing the technologies presented in previous chapters and summed in Figure 9, this section aims to compare and adapt these technologies to suit the scope of the thesis. Starting with the type of fuel cell, the high-temperature systems can be discarded, requiring hardware that cannot fit in small applications. Alkaline Fuel cells can also be rejected because of high operating pressures, temperatures, and cryogenic storage systems. Pan *et al* . (2019) consider polymer electrolyte membrane fuel cells and methanol fuel cells suitable for unmanned air vehicles. However, DMFCs practical operating voltage is still much lower than PEMFCs, primarily due to the methanol crossover phenomenon.

Subsequently, among the various existing types of fuel cells covered, the PEMFC demonstrates being the most promising contender for powering UAVs. It has a quick start-up, high specific energy, a low optimum operation temperature, and it is the most studied and developed in a diversity of practical cases (Pan *et al* ., 2019).

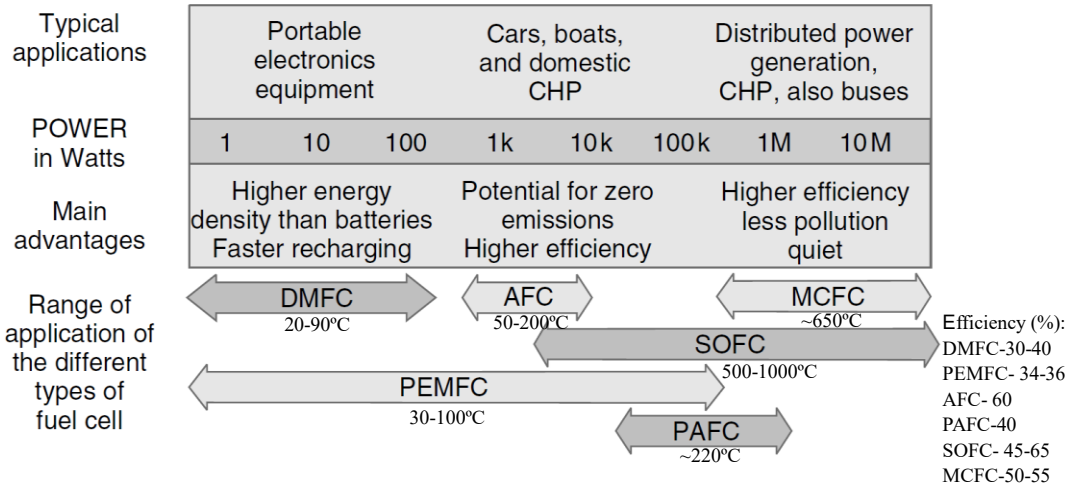

Figure 9- Chart summarizing the applications, main advantages. operating temperatures and efficiencies of fuel cells of different types, adapted from (EG&G Services, 2000; Larminie & Dicks, 2003; Rayment & Sherwin, 2003)

In terms of propulsion system configuration, the characteristics of a hybrid system suit better a military UAS than those of a pure hydrogen system for its high endurance and quick response to power peak variations. Considering the nature and performance demands of PAFs missions, and the reasoning in 2.2.2., a hybrid system is superior. Furthermore, hybrid systems provide redundancy, both in terms of payload and onboard subsystem energy, as well as propulsive energy.

The variety of missions demanded in the operational goals of the PAF indicate that atmospheric surroundings will not be constant in some flight conditions. High altitude missions mean less air density, which means degraded cell efficiency due to the hindered oxygen supply, increasing activation losses. Studies such as Atkinson *et al* ., (2017) point to a drop in maximum power from 2.21 W to 1.83 W by climbing to 3239 m. Firefighting surveillance missions mean that the aircraft may have to operate in areas of smoke that pollute the cell's components.

This operational constraint allied with the H_2-O_2 advantages presented in the previous chapter point to leverage the latter type of systems for UAS over an air-based supply. However, a lack of evidence in the efficiency gained/ added weight ratio point to a knowledge gap that can be significant in UAS propulsion. In this regard, further research is required.

2.3 PEMFC as Aircraft Power Supply

In March 2008, Boeing Company tested the first manned fuel-cell powered aeroplane in history. The hybrid power system comprised a 24 kW PEMFC stack and a Li-ion 50-75 kW battery for take-off and climb only. The aircraft cruised for 110km, 1000m above ground level for *ca.* 28 minutes in the missions – the estimated total endurance was one hour (Lapeña-Rey *et al*., 2010).

Since then, various researchers successfully developed PEMFC powered UAS demonstrators, with increasing power and endurance. (Bayrak *et al* ., 2020; Bradley *et al* ., 2007; Lapeña-Rey *et al* ., 2017; Pan *et al* ., 2019; Swider-Lyons *et al* ., 2011; Yang *et al* ., 2016). Nowadays, many commercial companies such as Intelligent Energy, Northwest UAV and BCH Energy offer reliable options for UAV PEM fuel cells.

2.3.1 Required Hardware

The PEM stacks are composed of Membrane Electrode Assemblies (MEAs), bipolar plates, current collectors and endplates. However, proper conditions must be assured for this power system to work effectively, requiring several auxiliary components. These supporting components and auxiliary systems are identified as the balance of plant (BoP) (Büchi *et al* ., 2007; Larminie & Dicks, 2003).

Fuel and air must be circulated through the stack by compressors and blowers in larger applications. Often, compressors are used to optimise the reactions, allowing precise control of working pressures. Different type of compressors can be applied, such as roots, screw, centrifugal, radial, or axial flow compressor. The use of intercoolers is also common (Carrette *et al* ., 2000). Fans and blowers are also a way to cool the fuel cell, and axial fans are often used.

Electric motors are the main component of the propulsion system and drive the blowers and compressors, utilising the energy generated by the stack. Then, an electronic conditioning system is necessary to meet load requirements. DC/DC converters can be used to extend the range of operating voltages or provide specific voltage values.

Proper humidification of polymeric membranes is important. At moisture levels below recommended values for each system, ionomer water content falls, reducing conductivity and adversely affecting the kinetics of reduction and oxidation reactions. In that manner, a gas humidification system is required to control this variable, at least in the cathode line (Kunusch *et al.*, 2012).

Hydrogen storage is a matter of active research, the main options are compressed gas, cryogenic liquids and solid metallic hydrides. Additional control valves and pressure regulators are required to control the flow to the cell.

2.3.2 Weight Management

Weight management is crucial in UAS applications. In 2007 and 2011, Bradley *et al* .(2007) and Swider-Lyons *et al.* (2011), respectively, developed fuel cell powered aircraft demonstrators. The BoP used by Bradley *et al* ., could be divided into thermal management, air management, and hydrogen storage and management subsystems (Figure 10). The aircraft had an endurance of 43min and featured a 500W FC.

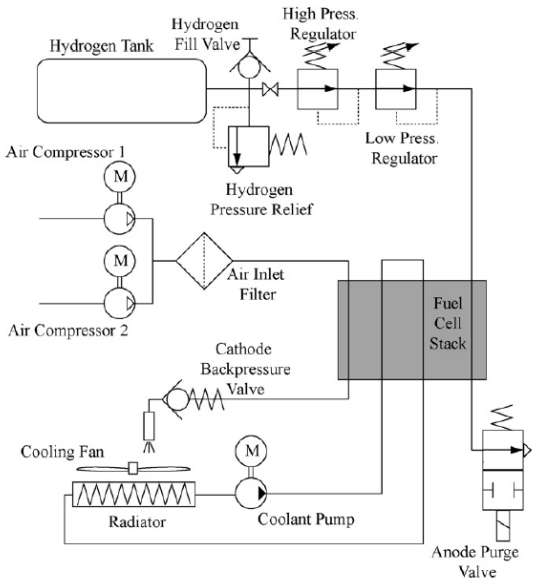

Figure 10- Fuel cell system diagram in aircraft, as per Bradley et al ., (2007)

Swider-Lyons designed the Ion Tiger within the constraints of a 5 lb (2.3 kg) payload (representing 14,3 % of Take Off Gross Weight (TOGW)) 300W cruise power and 24 h endurance. The weight distributions in both aircraft are specified in Table 1. Swider-Lyons results revealed to be significatively better, showing the advances made in just four years (Bradley *et al* ., 2007; Swider-Lyons *et al* ., 2011).

Table 1- Weight distribution of the demonstrators, presented in the format: Component weight [% of TOGW] (Bradley et al ., 2007; Swider-Lyons et al ., 2011)

	Weight				
Aircraft	**Electric engine**	**Fuel cell**	**Fuel tank / Fuel**	**BoP**	**TOGW**
Bradley Demonstrator	0.49 kg [3 %]	4.96 kg [30 %]	1.187 kg / 0.148* kg [8 %]	3.641 kg [22 %]	16.1 kg
Swider-Lyons Ion Tiger	0.48 kg [3 %]	0.99 kg [6 %]	3.62 kg / 0.5 kg [26 %]	3.641 kg [22 %]	16.4 kg

* Approximately calculated value, not specified in the article

2.4 Fuel Cell Degradation

Reduction in cell performance, caused by chemical and physical degradation phenomena, limits PEMFC durability and hinders its performance over time (Gazdzick *et al* ., 2016).

Poisoning can trigger some degradation mechanisms. The most significant are the following (Yuan *et al* ., 2011):

- Kinetic effect, caused by the poisoning adsorption of both anode and cathode catalyst sites, blocking them and reducing the electrochemical surface area (ECSA).
- Conductivity effect, caused by impurities accumulation in the membrane and ionomer, lowering of protonic conductivity.
- Mass transfer effect, due to deviations in the structure and hydrophobicity of the CLs and/or GDL.

The degradation of the GDL is often due to the loss of hydrophobic agents like polytetrafluorethylene (PTFE), resulting in a decreased water management capacity and increased mass transport resistance of the cell. These different degradation phenomena, also described by de Bruijn *et al* ., (2008), negatively influence the power density of the cell.

Several authors studied the output impact of different gas contaminants in fuel cell supply, namely nitrates and sulphites, (Jing *et al* . (2007), Hongsirikarn, (2010), Uddin *et al* . (2015), and Nagahara *et al* ., (2008)). Nagahara *et al* ., (2008) established that sulphur compounds cause the most severe performance loss, which can be attributed to kinetic losses. The same study also suggested that high relative humidity (RH) operation resulted in almost complete recovery in performance. St-Pierre (2011) studied the cation exchange with ionomer protons and came to the conclusion that in the potential range of PEMFCs (0.6–1 V) nitric oxides are almost exclusively adsorbed as NO due to the stability range of the molecules.

The CO contaminations in the hydrogen supply has been widely debated in literature, (Valdés-López *et al* ., (2020), Jiménez *et al* ., (2005) and Pérez *et al* ., (2014)). Pérez *et al* ., (2014), recorded, with one ppm CO in the anode and 70% fuel utilization, a 50 mV drop (representing 10 % initial voltage) in 50 minutes. However, literature is scarce in air stream

carbon monoxide contaminations. Only Moore *et al* ., (2000) conducted a comparable experiment, accessing the effect of various contaminants, including CO, on the air intake, recording 4% reversible performance drop at 20ppm in 15 min.

Likewise, only a few authors studied the influence of salt particles in the cathode air stream, (Mikkola *et al* ., (2007); Uemura *et al* ., (2017) and Yan *et al* ., (2011)). The authors registered, a decrease of effective surface area of the platinum catalyst by 22.6%, and in long operation time a declination rate of 1,082 mV/ h for NaCl air fuel gas mixture, in separate experiments.

The presence of contaminates in the atmosphere that can degrade the performance of the cell can be a determining factor in the H_2/O_2 vs H_2/Air deliberation, described in chapter 2.2.3., as recurring UAS fleet missions such as wildfire and maritime surveillance take place in an environment with atmospheric conditions far from the standard. Table 2 summarizes the FC performance loss in the presence of contaminates in the cathode and anode.

Table 2- Contaminations in literature summary

Contamination	Admission Mean	Possible Operational Cause	Result	Reference
NaCl	Direct Solution Admission in cathode	None	Irrecoverable 33 % performance loss in 100 h	(Mikkola *et al* ., 2007)
	Salt Crystals in cathode (Ultrasonic vibrations + heated pipeline)	Operation in dry salt-rich environment	ECSA decreased by 22.6 %	(Uemura *et al* ., 2017)
	Sea water vapours in air stream	Sea surface operation	50 % performance decay in 48h, full recovery after 40 h clean air	(Sasank *et al* ., 2016)
	Fine mist in air supply	Sea Operation	No significant influence	(Yan *et al* ., 2011)
COx	Carbon monoxide cathode admission	Wildfire operation	4 % reversible performance drop at 20 ppm in 15 min	(Moore *et al* ., 2000)
	Carbon monoxide in hydrogen supply	Impurity in H_2 tank	18 % reversible performance drop at 100 ppm in 5h	(Jiménez *et al* ., 2005)
			10 % performance drop in 50 min	(Pérez *et al* ., 2014)
NOx/ SOx	SO_2/NO_2 in air admission	Wildfire operation	35 % partially reversible performance loss at 1 ppm SO_2 in 100 h	(Jing *et al* ., 2007)
			10 % reversible performance loss at 1 ppm NO_2 in 100 h	

Chapter 3 Materials and Methods

This chapter describes the preparation of the test process, defining the methods, techniques, materials, and samples used, the optimal working conditions and the general characterisation of the tested systems.

3.1 Test Bench and Cell specification

The setup used in the experimental study, seen in Figure 11 and Figure 12, was composed by an oven (Termolab) to control the cell temperature. The gases were fed to the cell using mass flow controllers (Alicate Scientific). The humidification of the gases was assured using two bubblers and two high performance liquid chromatography (HPLC) pumps that allow humidification ranging between 0-100 %. Two separate condensers, followed by two pressure controllers (Alicate Scientific), allow the pressure control of the cell. The unit was controlled using a LabView software interface.

For the electrochemical characterisation and data recording, the equipment used in a first phase was a Zahner potentiostat IM6e and a PP240 load. This equipment was then replaced by the newer versions, Zenium PRO potentiostat and PP241, which were used to complete the remaining tests. For characterization and data acquisition control, the Thales software was used.

At the start of the experimental stage of the thesis, the installation of a new testing stand was started at the Laboratory for Process Engineering, Environment, Biotechnology and Energy (LEPABE) at FEUP. This test bench will be able to fully characterize fuel cells and electrolysers, both for stacks and individual cells – further details on this system can be found on Appendix A.

However, due to delays in material delivery, the project could not be finalized in time for the start of the contamination tests. Hence, the existing installation described above was used.

Figure 11- Test bench overview: 1- Zenium PRO potentiostat; 2-Additional control box; 3-PP241; 4- Flow and Pressure controller board; 5- Anode HPLC pump; 6- Cathode HPLC pump; 7- Scientific oven series 2000 for cell temperature control; 8- Water deposit

Figure 12- Open oven: 1- Oven control interface; 2- Anode Bubbler; 3- Cathode Bubbler; 4- Fuel cell

The membrane used for all tests was a Quintech® Nafion 212 (MEA-H50-N212), with 50 cm^2 of active area (7.23 x 7.27 cm), 60 µm membrane thickness and a loading of 0.6 mg/cm² Pt and 0.3 mg/cm² Pt, for the cathode and anode, respectively. A summary of the membrane specifications can be found on Table 3, and a polarisation curve and optimal working conditions provided by Quintech can be found in Figure F - 1. The remainder cell structure, flow fields, current collectors and end plates are experimental and were designed by Pragma Industries® for FEUP.

Table 3- Membrane specifications summary

	Quintech® Nafion 212
Catalytic Active Phase	Pt supported on carbon
Active Area	50 cm² (7.23 x 7.27 cm)
Cathode Catalytic Loading	0.6 mg/cm² Pt
Anode Catalytic Loading	0.3 mg/cm² Pt
Membrane Thickness	60 µm
GDL Thickness	235 µm

3.2 Contamination Tests

As part of the PAF UAS missions we have operations in maritime search and wildfire environments. Therefore, two categories of tests were conducted to test the PEMFC performance under these possible hazardous environments. Sodium chloride (NaCl) and carbon monoxide (CO) / nitric oxide (NO) were the chosen pollutants to simulate seawater and wildfire contaminations, respectively.

Many researchers usually perform fuel cell tests with higher contaminant concentrations than the ones recorded in the atmosphere. This method accelerates cell voltage degradation and ensures that results are easier to interpret, minimising the influence of other degradation mechanisms. However, extrapolations of the contamination effects to lower concentrations for predictive purposes should be interpreted with caution, as they may be misleading due to the existence of non-linear dependencies (St-Pierre *et al* ., 2014).

In this sense, this work seeks a different approach, starting with contamination values that recreate the concentrations recorded in the atmosphere, and gradually progressing then to higher values, which accelerate the contamination effects. All contamination periods were conducted between 15 and 20 hours and were repeated to assure consistency.

The NaCl contaminant tests were conducted based on recordings by the following authors: (Blanchard *et al* ., 1984; Blanchard & Woodcock, 1980; Mikkola *et al* ., 2007; Smirnov *et al* ., 2003). All recorded sea salt aerosol concentrations in maritime conditions, present in the articles mentioned above, ranged from 500 to 800 nmol / m^3, depending on the weather conditions, altitude levels and wind velocity. The first value - 500 nmol / m^3 - was used to better reflect sea salt levels at 100 m altitude or above.

The cathode side pump injected a NaCl solution into the air steam. Calculations were made to determine the concentration of the solution injected into the bubblers in order to have a 500 nmol / m3 in the cathode air supply. The two subsequent contaminations were chosen to gradually reach a value of contamination with visible influence on the cell's performance.

For the wildfire experiments, atmospheric data was used to obtain a simulated environment closer to reality, in coordination with the SmokeStorm project, from the *Associação para o Desenvolvimento da Aerodinâmica Industrial* (ADAI), part of the University of Coimbra. Through surface and altitude data recorded by ADAI, an estimated value was calculated of the concentrations of the main gases released in a wildfire present at 100 m AGL. The values obtained were 13 ppm for carbon monoxide (CO) and 1 ppm for nitric oxide (NO) (Miranda, 2004; Miranda *et al*., 2005, 2010, 2012; Valente *et al*., 2007).

For the CO and NO tests setup, a compressed bottle of diluted gas was connected through a T-connector to the air supply. Contaminant fraction in the mixture was regulated through a separately set mass flow controller. The contaminant concentration was then increased to better understand its effect in the cathode feed supply.

Besides the addressed gases, SOx and other nitric compounds such as NO_2 were also a possible contamination source, as seen in Section 2.4. However, tests were not performed regarding these contaminants, due to gas unavailability and long expectancy period in deliveries.

3.3 Characterisation Techniques and Procedures

3.3.1 In-situ Electrochemical Techniques

3.3.1.1 I-V Curves

A fuel cell performance is best summarised by its current-voltage response. I-V curves, or polarisation curves, show the voltage output of the fuel cell for a given current density loading. In this thesis, the curves were obtained using the load in galvanostatic mode, monitoring the potential, from open circuit voltage (OCV) to high current densities (0.7 A/cm²), in pre-established current points, with retention times of one minute. The polarisation curves for each life stage were obtained using fixed hydrogen and air flowrates (calculated to 1 $A \cdot cm^{-2}$). Current densities above 0.7 A/cm² was not studied due to equipment limitations.

3.3.1.2 Voltage Degradation

The degradation tests were conducted in galvanostatic mode at current density of 0.4 A/cm², during 15-20 hours in each contamination value and were repeated at least one time to assure validity and consistency in results.

3.3.1.3 Cyclic Voltammetry

A cyclic voltammogram is obtained by measuring the current at the working electrode while cycling the induced potential. The working electrode chosen was the cathode, and CV tests were performed using the same equipment as the one used in the I-V curves, in the Thales program.

A gas flow of 200 mL/min of H_2 and N_2 was fed to the anode and the cathode, respectively, and standard test operating conditions were applied. The electrochemical surface area (ECSA) is calculated accordingly to equation 3.1, in which qPt is the charge density obtained from the CV, L is the Pt loading in the electrode, and Γ is the charge required to reduce a monolayer of protons.

$$ECSA = \frac{q_{Pt}}{\Gamma \cdot L} \quad [3.1]$$

3.3.1.4 Electrochemical Impedance Spectroscopy (EIS)

EIS allows the distinction of the different sources of losses in the cell, described in 2.1.2. Impedance is a measure of the ability of a system to impede the flow of electrical current, and impedance measurements are usually made by applying a small sinusoidal voltage perturbation and monitoring the system's resultant current response (O'Hayre *et al.*, 2016). EIS were obtained between 100 mHz and 100 kHz with a perturbation amplitude of 5 mV.

3.3.2 Ex-Situ Physical Techniques

3.3.2.1 Scanning Electron Microscopy (SEM)

Through a focused beam of high energy electrons, scanning electrode microscopes produce complex, high magnification images of the surface topography of a sample. This technique allows identifying changes in the microstructure of the membrane electrode assembly. After the NaCl contamination tests, it was used to scan the membrane and GDL for salt crystals and to monitor changes in cross-section membrane thickness.

3.3.2.2 Temperature Programmed Desorption (TPD)

The TPD is an analysis method in which the sample is heated at a linear heating rate under a carrier gas flow, and the change of the reaction gas that is desorbed from the surface upon heating is monitored with a downstream detector as a function of temperature (Ishii & Kyotani, 2016).

In this thesis, TPD was used to analyse the presence of CO adsorbed in the catalyst layer of anode and cathode. The CO adsorption was studied by CO_2/CO temperature-programmed desorption combined with mass spectrometric analysis (CO_2/CO-TPD-MS, ChemBET Pulsar TPR/TPD). Afterwards, the CO_2/CO desorption was monitored using a quadrupole MS (Pfeiffer Vaccum OmniStar GSD 320) in the temperature range of 50 – 700 °C, and a Thermal Conductivity Detector (TCD).

All tests were conducted in the same conditions. The inert gas used was helium, at a 20 mL/min gas flow. The sample was heated at 10 K/min, from room temperature to 1173.15 K.

3.3.2.3 Inductively Coupled Plasma Mass Spectrometry (ICP-MS)

ICP-MS is a highly sensitive tool for target-element orientated detections of relevant and unknown compounds. It can provide accurate and reliable information on concentrations and species identity, by coupling to highly selective separation and reference compounds (Ammann, 2007).

This technique was used to analyse the MEA for NaCl traces after salt contaminations. Three samples were analysed, one from a clean MEA, and two from salt contaminated MEAs. Before the analysis, a digestion of the sample was conducted, which was achieved by dissolving the sample with 7 mL of HNO_3 65 % and 1 mL of H_2O_2 30 %, while being on a microwave programmed to reach a temperature of 200 ºC after 15 min of being turned on, and remaining at that temperature for a duration of 15 minutes, followed by a cool down to ambient temperature.

3.3.3 Test Protocol and Optimal Operating Conditions

The first step was to measure the relative humidity of the gas at the cell entrances, to ensure the desired humification. A hygrometer (Vaisala® Dewpoint Meter DM70) was mounted on the cell entrance, and the chosen value for both anode and cathode was 100 % RH, regulated by the HPLC water flow.

A break-in procedure is necessary to activate the cell and bring it to stable operating conditions, being a fundamental step to execute before tests. Break-in or conditioning guarantees that the cell potential will be stable before the test initiation. The activation was made at 70 ºC, fixed voltage, starting at 0.8 V and gradually descending to 0.65 V, in a total of 20 hours.

The initial planning of the contamination tests consisted of the beginning of life (BoL) electrochemical characterisation, followed by three contamination stages. Afterwards, a recovery period was conducted, proceeding each stage, which was achieved by feeding pure water on the cathode side air gas entrance. Upon each contamination or recovery, a middle-life characterization was conducted.

However, this configuration of tests revealed lack of stability in the cell performance, which can be observed in Figure D-1, present in the Annex D. Indeed, the figure shows peaks at the start of every set of contaminations, in *current vs time* graph, which can be attributed to hydrogen accumulation in the anode due to test disruption, when performing mid-life characterization, caused by a sudden shut down of the potentiostat.

After this first trial, additional tests were conducted to optimise the MEAs performance and stability. These tests resulted in alterations in the working conditions of the tests, namely the anode and cathode working pressure, from 1.25 to 2 bar due to the higher system stability recorded at higher pressure; the fixed long test voltage, from 0.6 V to 20 A (0.4 A/cm^2)-galvanostatic mode; and removal of middle-life characterisations, for a more stable and continuous contamination cycle. These working conditions were then applied in the final configuration used during contamination tests. A summary of the operating conditions used, can be found in Table 4.

Table 4- Optimized operating conditions for contamination tests. A, B, C, D and E refer to different EIS tests.

	Long Tests	**I-V Curves 0.5A/cm2**	**I-V Curves 1A/cm2**	**EIS**	**CV**
System Temperature	70 ºC	70 ºC	70 ºC	70 ºC	70 ºC
Cathode Flow Rate	0.8 L min^{-1} Air	0.8 L min^{-1} Air	1.7 L min^{-1} Air	0.8 L min^{-1} Air	0.2 L min^{-1} N_2
Anode Flow Rate	0.2 L min^{-1} H_2	0.2 L/min H_2	0.4 L min^{-1} H_2	0.2 L min^{-1} H_2	0.2 L min^{-1} H_2
Cathode Pressure	2 bar	2 bar	2 bar	2 bar	1.5 bar
Anode Pressure	2 bar	2 bar	2 bar	2 bar	1.5 bar
Cathode HPLC Water Flow (%RH)	0.12 ml min^{-1} (100%)	0.12 ml min^{-1} (100%)	0.12 ml min^{-1} (100%)	0.12 ml min^{-1} (100%)	0.03 ml min^{-1}
Anode HPLC Water Flow (%RH)	0.03 ml min^{-1} (100%)	0.03 ml min^{-1} (100%)	0.03 ml min^{-1} (100%)	0.03 ml min^{-1} (100%)	0.03 ml min^{-1}
Fixed Potential/ Current	0.7 V / 20 A (0.4 A cm^{-2})			A- 1 A B- 10 A C- 20 A D- 0.7 V E- 30 A	
Disturbance Amplitude				A- 50 mA B- 200 mA C- 500 mA D- 5 mV E- 1 A	
Scan Rate					20 mV/s (3 cycles)
Stoichiometry	H_2: λ=1.2; Air: λ=2				

Electrochemical characterisation, composed of two polarisation curves, four EIS and one CV, was made at the BoL of the cell; once the contamination was completed, these electrochemical tests were also performed at the end-of-test (EoT). Later on, the equipment used on the testbench was updated by Zenium PRO potentiostat and PP241, which allowed to achieve higher current densities for the I-V curves. Therefore, a new EIS test was introduced at 30 A (0.6 A cm^{-2}).

After BoL tests, the first contamination stage was initiated. For the tests mimicking a PEMFC subjected to a maritime environment – **NaCl contaminations** - the fuel cell was operated for 20 hours with a contamination solution of 0.1 mg/L NaCl injected in the cathode at 0.23 ml/min. A fixed voltage of 0.7 V was chosen after the first cycle, since it was the most stable potential for the membrane in these tests. After this stage, the procedure was repeated for the solution concentrations of 10 mg/L and 10 g/L. This cycle was then repeated in fixed current density to assure reproductivity.

The cell was operated in constant potential and constant current density modes, during the life test, to avoid significant changes in cathode potential due to performance decay. Small periodic stops were made throughout the life test to increase the concentration of the solution in the bubblers. Two similar test cycles were recorded for reproducibility purposes, being the first at fixed voltage (0.7 V) and the following at fixed current density (0.4 A cm^{-2}). Tests were performed in distinct MEAs, both with the specifications present in chapter section 3.1, being similar in every other aspect.

Wildfire tests were sub-divided into CO and NO; cumulative tests were conducted with the most abundant available contaminants present in the atmosphere, 500 ft above a wildfire. After a BoL characterisation, three consecutive 20-hour tests were conducted at the concentrations of 13, 50 and 75 ppm for CO; for NO, 2 and 20 ppm concentrations were used, based on aforementioned literature. An anode CO contamination was the last test set performed, and the chosen contamination was 50 ppm in a short contamination/ recovery cycle. The concentrations, times, and layouts of each test sets are detailed in Figure 13. Some repeated tests data is omitted from chapter four.

The ppm values presented were achieved by the admission of 1, 2.9, and 6.2 ml/min of a 1% carbon monoxide bottle mixed with 831, 829, and 826 ml/min of reconstituted air, respectively. No periodic stops were made throughout the life test for stability purposes. Two similar CO contamination tests were recorded for reproducibility purposes, using two commercial MEAs, with the characteristics described in Table 3.

The first experiment consisted of three contaminations, the 13, 50 and 75 ppm of CO gas were added to the cathode inlet air stream, for 20 hours each. For the second experiment, 50 and 75 ppm of CO gas were added to the cathode inlet air stream for approximately 10 hours each. Apart from differences in the duration of the contaminations, both tests were similar in the operative conditions used.

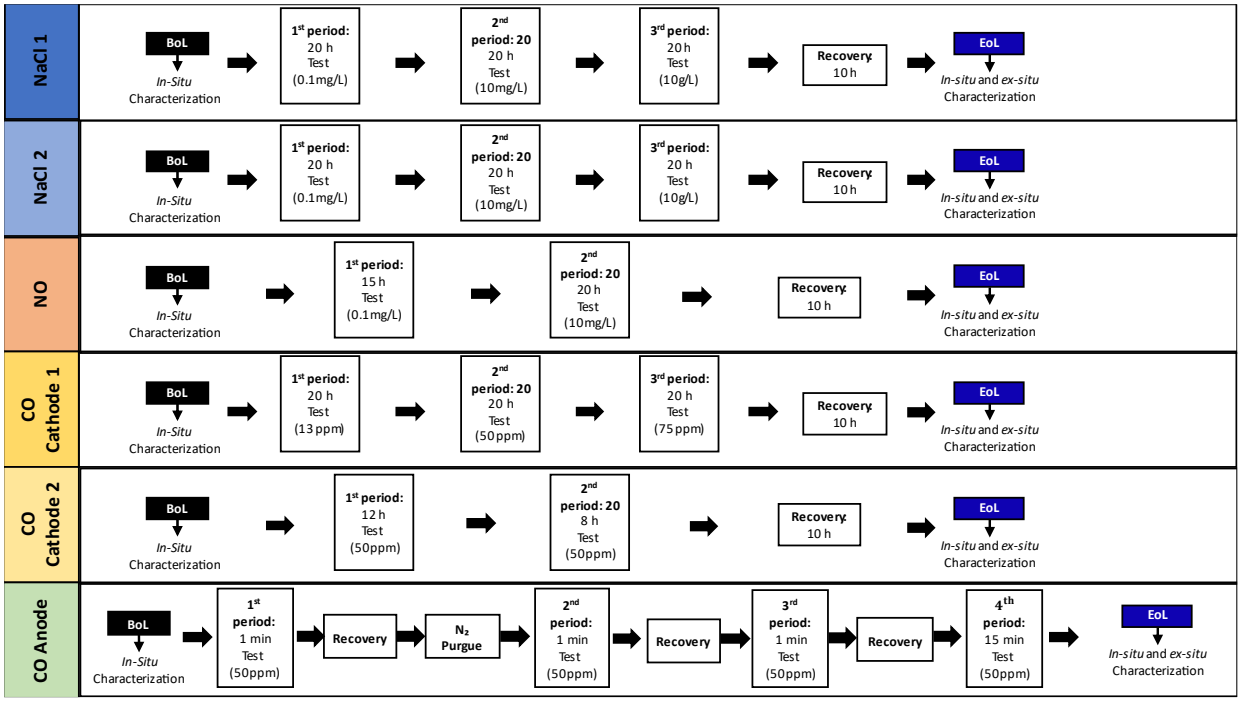

Figure 13- All contamination test protocol summary

INTENTIONALLY LEFT BLANK

Chapter 4 Results and Discussion

This chapter is divided into five Sections. In the first three, the results from the experimental contamination of the fuel cell will be presented, analysed, and discussed. In the fourth, the *ex-situ* tests will be analysed to support the degradation and characterisation tests and compared with literature results. The last section provides a comparative study of the different effects of the contaminations investigated.

4.1 Fuel Cell Performance Assessment

Before the contamination sets, a 20-hour activation and stabilization test was conducted to determine the MEAs performance in optimal operating conditions to compare it with contamination sets. This test was recorded using the same operating conditions as the contamination sets, except pure air was used. After the activation, the cell's performance was recorded for 20 hours, as represented in Figure 14.

Data shows a stable operation over time. The overall tendency of the system is a slight increase in potential of 0.2 mV h^{-1}, this behaviour points to a robust system.

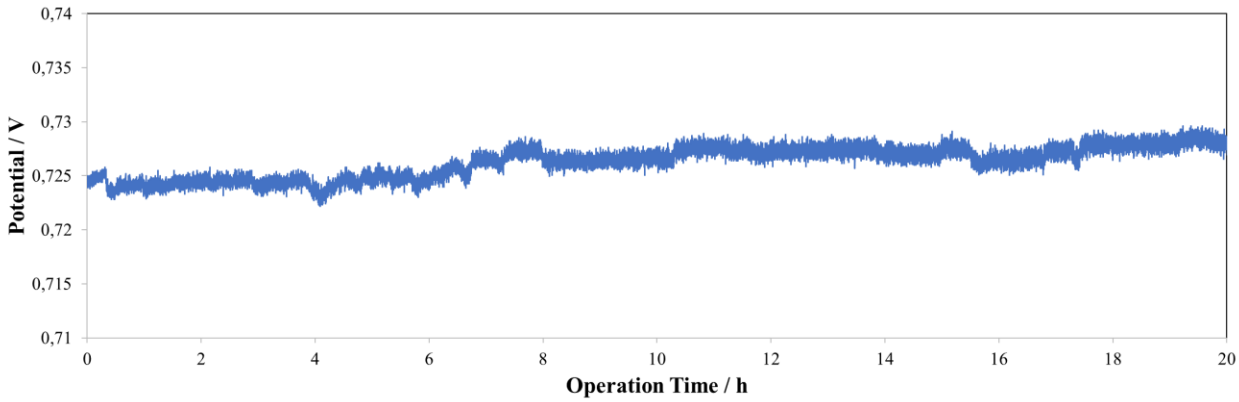

Figure 14- Potential evolution with operation time, for a current density of 0.4 A cm^{-2}, after 20 h activation.

4.2 Maritime Operation - NaCl Contamination

This contamination set aims to simulate fuel cell operation in a UAS operating above the ocean. The cycle tests regarding potential degradation and electrochemical characterisation, were performed with two commercial Quintech MEAs.

Three consecutive contaminations were introduced in the form of a NaCl water solution in the air side bubbler preceding the cell. This contamination admission method was chosen to simulate real operational conditions. The first contamination is based on collected data and simulates a fuel cell that is operated at 500 ft of altitude, being subjected to a saline atmosphere; The salt concentration was increased in the subsequent tests to study the cell performance degradation under severe conditions.

Figure 15 shows the *voltage vs. time* response of an operating fuel cell exposed to NaCl, at 0.4 A cm^{-2}. The contamination started at t = 0 h, and the concentration values are labelled on the figure, represent the NaCl concentration in the solution present in the cathode side bubbler for the correspondent period.

This test set shows an initially stable performance, and subsequent performance loss, as the overall voltage drop is 0.3 mV h^{-1}. The instability in the last 40 hours is likely due to over humidification of the system.

This behaviour was fairly expected, as in the Mikkola *et al* ., (2007) experiment, the highest performance drop was 4 mA $cm^{-2}h^{-1}$, 13 times larger than the values recorded in this experiment. This discrepancy can be related to the admission method, as Mikkola injected the liquid solution directly into the cathode air stream, causing reversible degradation in the cell by accumulation of salt crystals in the GDL.

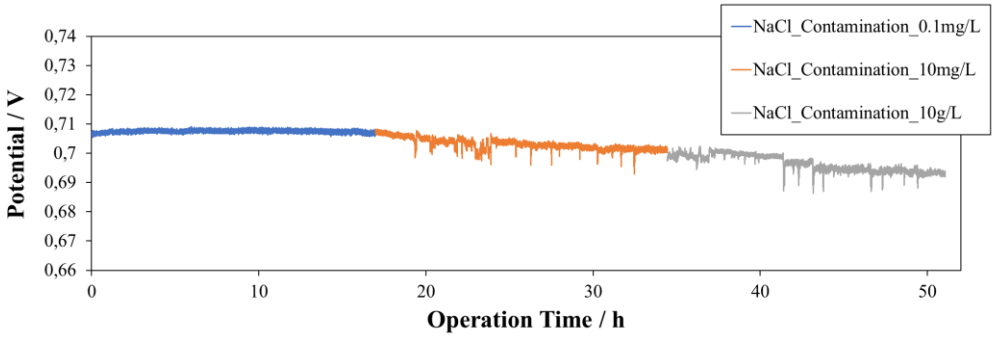

Figure 15- NaCl contamination: Potential evolution with operation time, for specific 0.4 A cm^{-2} A current density, with increasing NaCl contamination injection in the cathode, (concentrations of 0,1 mg L^{-1}, 10 mg L^{-1}, 10 g L^{-1} were added to the cathode side bubbler).

Figure 16, shows the polarisation curves recorded before (BoL) and after (EoT). The results indicate that effect of the contamination with salt at 0.4 A cm^{-2} was negligible. This leads to the assumption that salt is inert and do not affect the MEA, as the performance remained the same.

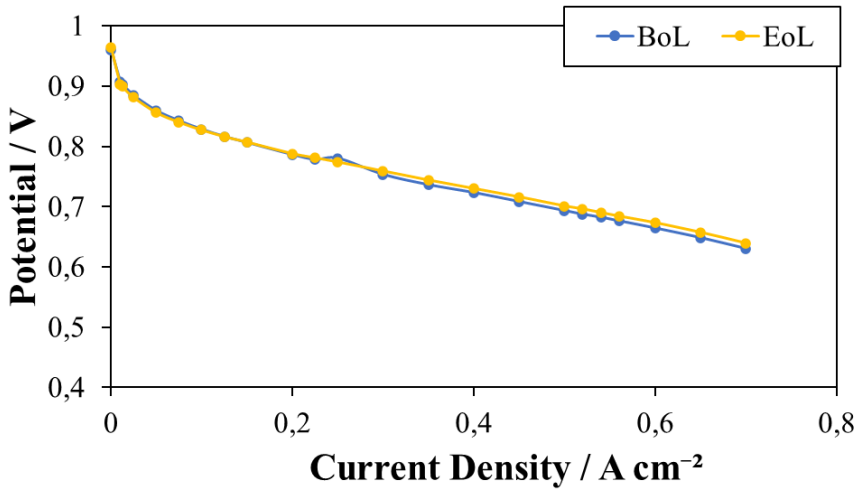

Figure 16- Descending Polarisation curve in BoL and EoT salt contamination characterisation sets 1 A/cm².

EIS analysis was conducted before and after salt contaminations at different current densities, Figure 17. No substantial changes were observed, neither in the ohmic nor in the charge transfer resistances. The ohmic resistance was constant throughout the experiments, being around 100 mΩ cm².

Notwithstanding, some instability is found in the low-frequency arc across the concerning tests, and in the graph E of Figure 17, performed at high current density (0.6 A cm^{-2}), the arc of the Nyquist plot increased. This suggests that a slight intensification of mass-transport resistance can be observed for high currents, although this is not observable in any other current densities; which can be related to an accumulation of water on the cell, blocking the active catalyst sites, hindering the mass transport of the reactants towards the Pt catalyst.

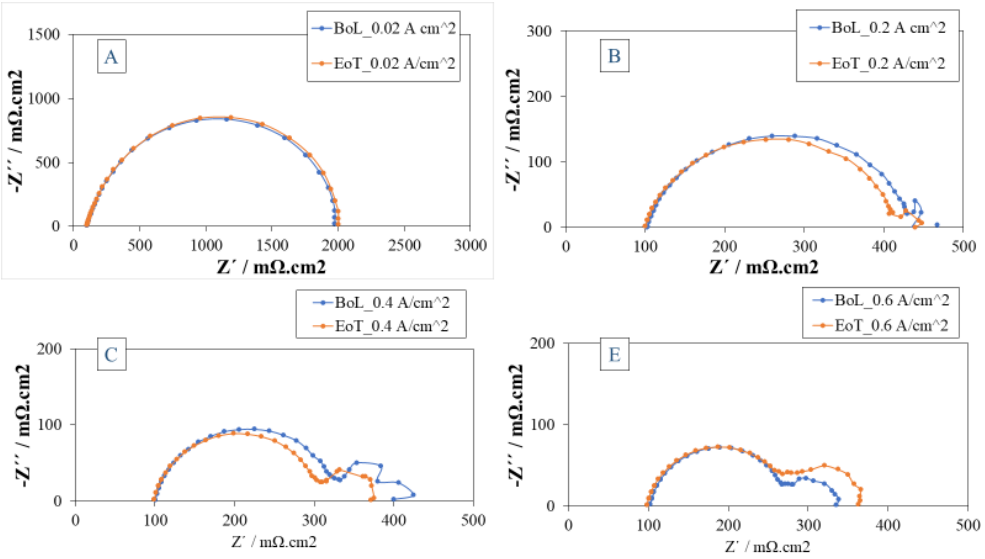

Figure 17- EIS Nyquist plots performed at the BoL and EoT characterisation, being performed at A) 0.02 A cm^{-2}, B) 0.2 A cm^{-2}, C) 0.4 A cm^{-2} and, E) 0.6 A cm^{-2}.

CV measurements before and after salt contaminations can be observed in Figure 18. After calculating ECSA from equation 3.1, a slight decrease from 12.4 to 11.5 m_{Pt}^2 g_{Pt} was recorded. This ECSA reduction is not significant and should account with the normal operation cell degradation.

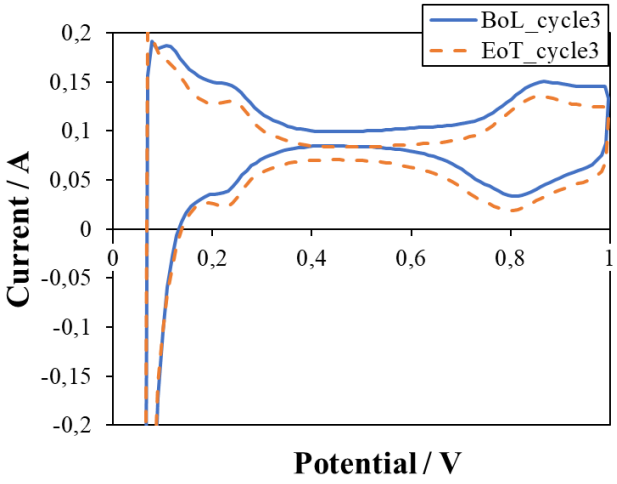

Figure 18- Cyclic voltammetry plots performed for NaCl contamination experiments, for the BoL and EoT. Cyclic voltammetry was performed at 20 mV s^{-1} scan, with 200 mL of H_2 and N_2 feed, for the anode and cathode, respectively.

4.3 Wildfire Operation - CO and NO Contamination

This contamination set aims to simulate fuel cell operation in an UAS in wildfire conditions. In this section, cycle tests results regarding potential degradation and electrochemical characterisation, performed with two commercial MEAs, will be analysed. Additionally, for comparison and validity purposes, a CO contamination was conducted in the anode, simulating an impurity in the hydrogen tank, this set is detailed in Apendix C.

This section is divided into CO and NO tests conducted separately. Few comparisons can be found on the literature for cathode carbon monoxide contamination, so some comparisons will be established taking in consideration the results of similar CO contamination tests, conducted in the anode side of the PEMFC.

4.3.1 CO Cathode Contamination

Two CO contamination tests were recorded for reproducibility purposes, using two commercial MEAs. The first experiment consisted of three contaminations, of 13 ppm, 50 ppm and 75 ppm of CO, added to the cathode inlet air stream, for 20 hours each. The first contamination (13 ppm) is based on collected data by ADAI and simulates a working PEMFC in a 500 ft atmosphere, above a wildfire. The CO concentration was then increase in the two subsequent contaminations to access the performace under severe operating conditions. To validate the results obtained in the previous test, a second MEA was tested using a CO concentration of 50 and 75 ppm.

In Figure 19, the plot for *potential vs. operation time* is presented. In the first 45 hours of operation, the performance decay was significant, averaging 0.5 mV h^{-1}. When the CO concentration was increased to 75 ppm, instability of the system was observed, showing a performance decay of 2.6 mV h^{-1} CO concentration (75 ppm). After the CO contamination, pure air was fed and the performance recovered almost completely – data not shown.

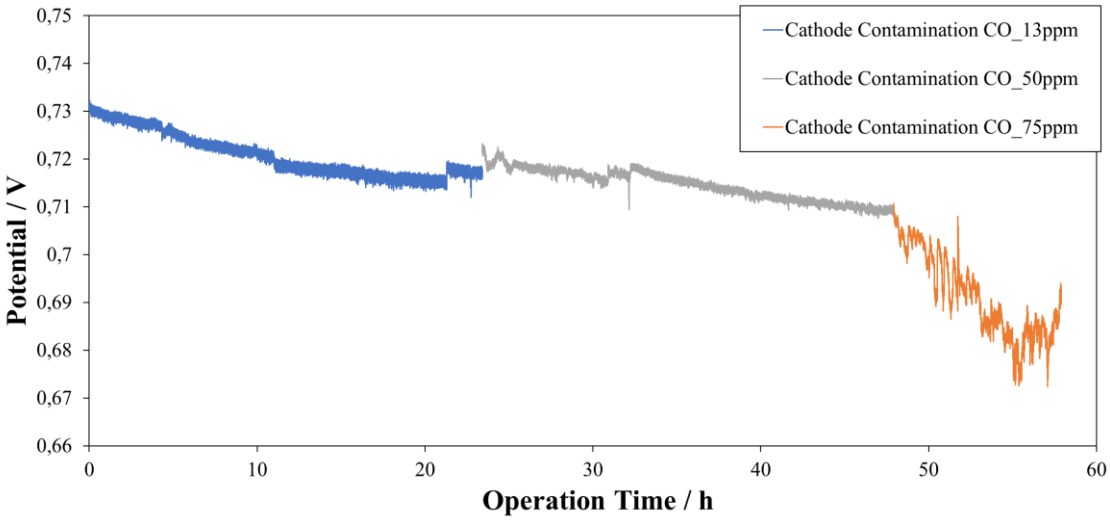

Figure 19- First CO contamination: Potential evolution with operation time, for specific 0.4 A cm^{-2} A current density, with increasing CO contamination injection in the cathode, (concentrations of 13 ppm, 50 ppm and 75 ppm of CO were added to the PEMFC air inlet).

To validate the results obtained in the previous test, the transition from 50 to 75 ppm was repeated, 12 hours in 50 ppm and 8 hours in 75 ppm. Figure 20 shows the results obtained, in *potential vs. time* plot. The performance decay averaged 0.38 mV h^{-1}, which is aligned with the previous result for the first 45 h. This suggests that a CO concentration of 75 ppm has some effect but is not a severe for the fuel cell performance.

Observing the anode side contamination results, present in literature, it would have been expected that carbon monoxide admission in the cathode, would have a significantly higher effect than the one obtained. In fact, Pérez *et al* ., (2014), obtained a potential degradation of 50 mV in 10 minutes by adding 1 ppm of CO on the anode H_2 inlet stream. The potential drop was attributed to the adsorption of CO onto the anode catalytic sites.

Nonetheless, the short bibliography referring to the cathode side CO contamination, pointed to a 4 % reversible performance drop at 20 ppm during a 15 min duration contamination (Moore *et al* ., 2000) In this study, for instance, a 10 % reversible performance drop was observed for 50 ppm, during 12 h test (Figure 20).

In subsection 4.4.2., a TPD analysis (temperature programmed desorption) and mass spectroscopy will be presented, to better assess the level of CO adsorption on the catalyst, by comparing the results of a pristine MEA with the ones of the MEA contaminated with CO.

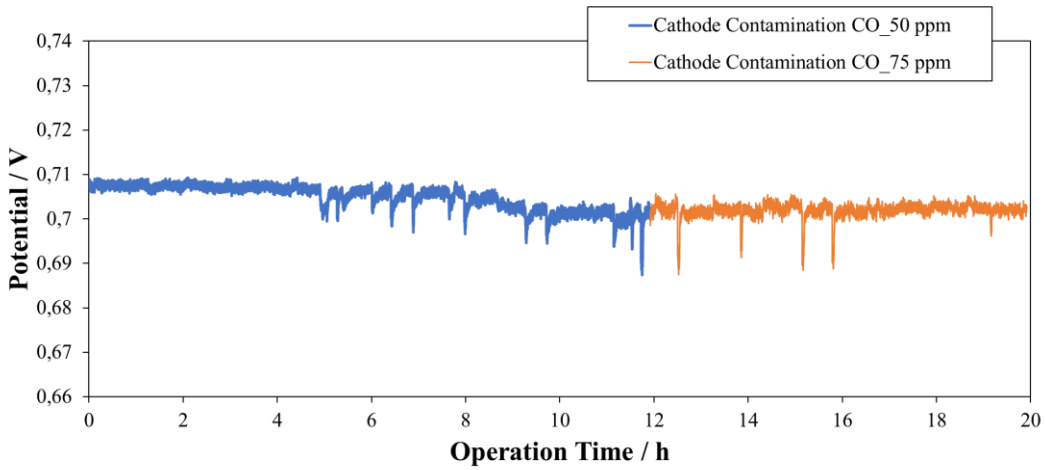

Figure 20- Second CO contamination: Potential evolution with operation time, for specific 0.4 A cm^{-2} current density, with increasing CO contamination injection in the cathode (concentrations of 50 ppm and 75 ppm were added to PEMFC the air inlet).

BoL and EoT test sets were recorded before and after the CO injection to analyse performance decay, catalyst poisoning and monoxide migration to the anode, seen in Figure 21. All characterisation techniques were recorded using the operating conditions specified in Table 4. It is noteworthy that the EoT electrochemical characterisation was recorded in clean air conditions.

In the I-V curve plot in Figure 21 for the second MEA, revealed a noteworthy degradation in the high current density range, while in the activation and ohmic area, the performance remained stable, indicating that the main effect of the contamination was in the mass transport region; at 0.7 A cm^{-2}, the voltage drop was 6.5 %, in which potential decayed from 0.64 V to 0.60 V, from the BoL to the EoT.

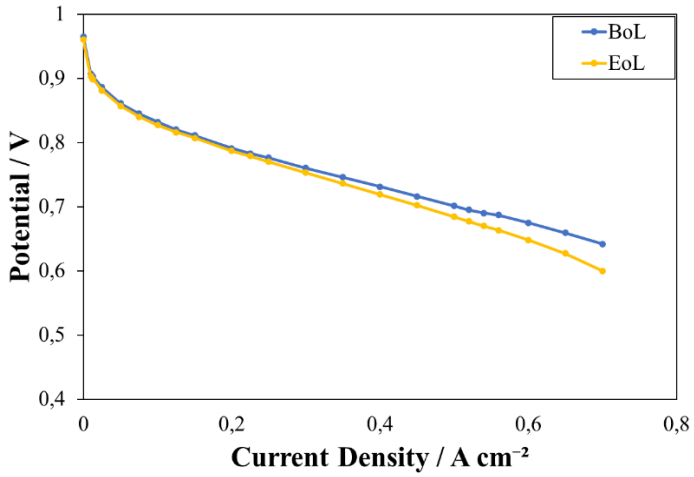

Figure 21- Second CO contamination: Descending Polarisation curve in BoL and EoT characterisation sets.

In Figure 22, show the Nyquist plots before and after the carbon monoxide contamination. As in the salt contaminations, the high-frequency arc remained stable, meaning this contamination had minimal effect on ohmic and anode charge transfer resistances. However, at high current densities the EIS (Figure 21-E) the mid/low-frequency region, related to cathode charge transfer resistances and mass-transport resistance seems to be affected. In fact, the second arch (mass-transport resistance) increased 12.5 %, from 80 mΩ cm^2, to 90 mΩ cm^2, from the BoL till the EoT).

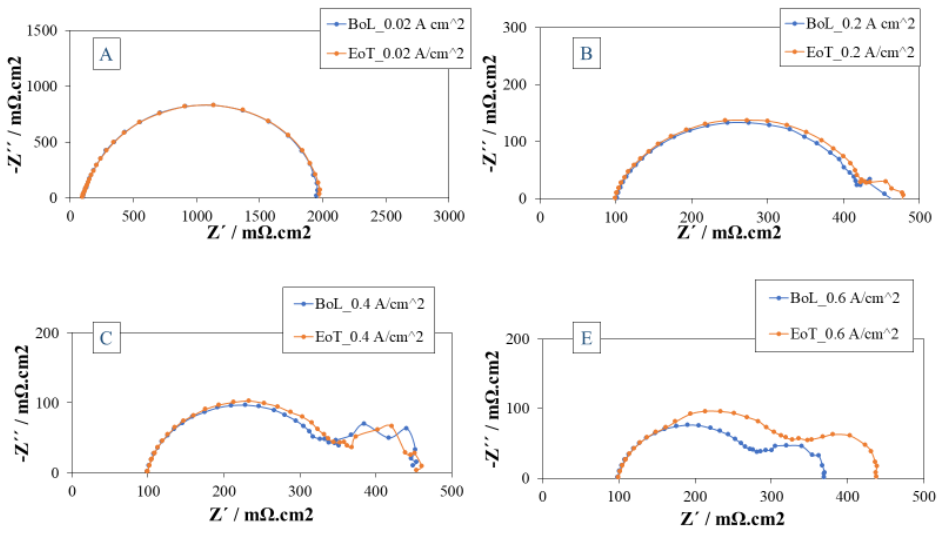

Figure 22- EIS Nyquist plots performed at the BoL and EoT characterisation for CO contaminations, being performed at A) 0.02 A cm^{-2} and 50 mA amplitude, B) 0.2 A cm^{-2} and 200 mA amplitude, C) 0.4 A cm^{-2} and 500 mA amplitude, E) 0.6 A cm^{-2} and 1 A amplitude.

CV measurements before and after cathode CO contaminations can be observed in Figure 22. ECSA suffered a significant reduction, from 11.5 to 9,9 mPt² gPt. This 14 % reduction was one of the largest recorded in test sets, and could be associated with CO adsorption in the CL, causing a significant blockage of catalytic sites, responsible for the slight performance drop verified in the I-V curves of Figure 20.

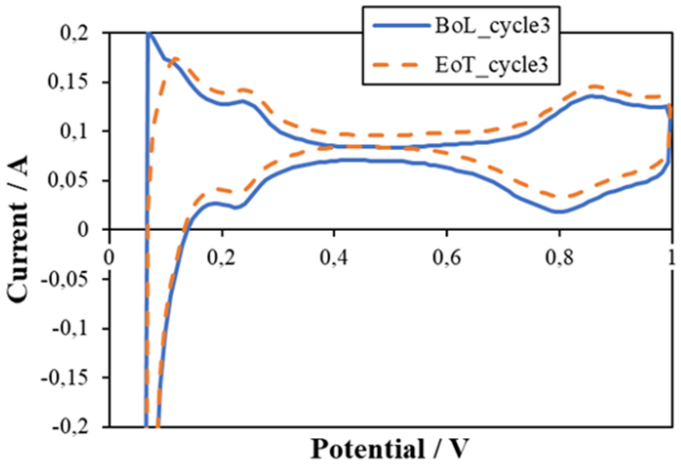

Figure 23- Cyclic voltammetry plots performed for CO contaminations experiments, for the BoL and EoT. Cyclic voltammetry performed at 20 mV s^{-1} scan, with 200 mL of H_2 and N_2 feed, for the anode and cathode, respectively.

Observing the results of the CO contamination on cathode, and despite not being the target of this study, a contamination of CO with a concentration 50 ppm was tested on the anode. The results are presented in Appendix C.

4.3.2 NO Contamination

Another common contaminant present in wildfires is nitric oxide. In this section, the effect of this contaminant in the performance of the fuel cell is detailed. The admission method of this contaminant in the cathode was similar to the CO experiments present in the previous subsection.

Two contaminations were administered into the cathode; the first of 2 ppm of NO, represent the values observed 500 ft above a wildfire (Miranda *et al*., 2005), and had a test duration of 15 hours; the second of 20 ppm of NO, aims to study the cell performance degradation under severe conditions, and had a duration of 25 h.

The NO contamination in the cathode, as can be observed in Figure 24, had little to no effect in the cell performance at the periods and concentrations investigated. No significant decay occurred in the contamination period. The overall potential decrease was -0.05 mV h^{-1}. From the scarce studies NO contaminations in the cathode, Talke *et al* ., (2018) recorded a 33 % performance drop in just 50 minutes at 10 ppm. Similarly, Misz *et al* ., (2016) recorded a average current loss of 67 % for 10 ppm NO in 130 minutes, while Jing *et al* . (2007) recorded 100 hours of NO_2 contamination at 1 ppm with another nitrogen compound, documenting a 10 % reversible performance loss.

Compared to the potential drop recorded in this 40-hour test, the degradations presented in the aforementioned references are very high. The fact that NO contaminations have little effect on the cell performance when compared to the Misz *et al* ., (2016) paper may be related to the stoichiometry of the fed gases being much higher - H_2: λ=2.3; Air: λ=6 2 in Minsk paper compared to H_2: λ=1.2; Air: λ=2 in this experiment- and the platinum loading of our MEA being lower - 0.4 mg cm^{-2} Pt on the cathode side and 0.1 mg cm^{-2} Pt on the anode side in Minks compared to 0.6 mg cm^2 Pt and 0.3 mg/cm^2 Pt in this experiment, respectively -.

Moreover, the tests in some of the bibliography were recorded using dry gases, which could affect just by itself, the fuel cell performance; moreover high humidity can attenuate contaminant

effect (Uemura *et al* ., 2017), this could explain the discrepancy. The humidity presented in this study presents RH values closer to UAS operation.

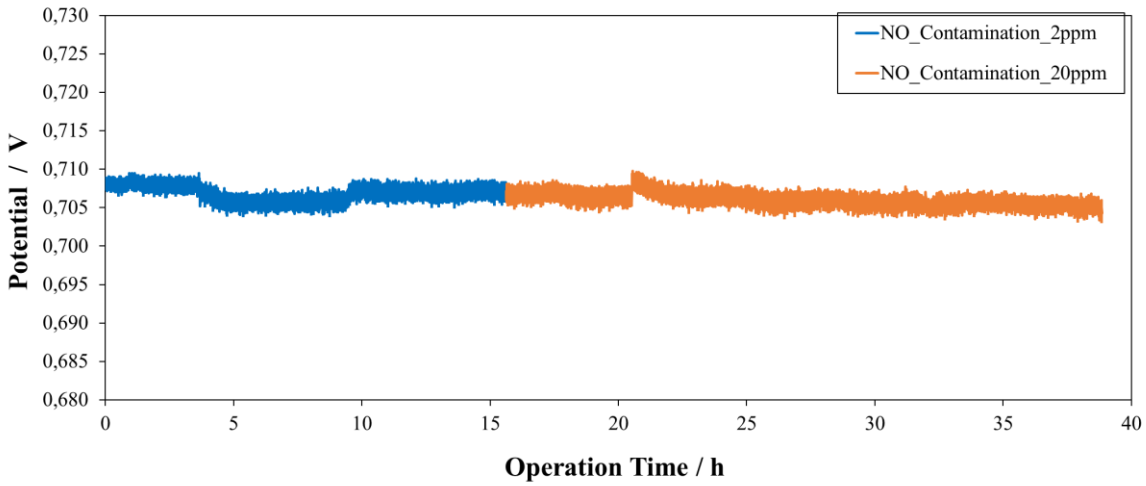

Figure 24- NO contamination: Potential evolution with operation time, for fixed 0.4 A cm^{-2} current density, with increasing NO injection in the cathode (concentrations of 2 ppm and 20 ppm of NO were added to the air inlet stream).

BoL and EoT test sets were recorded before and after the NO contamination. The contamination and characterization procedure and techniques are reported in Table 4. The I-V curves recorded show curious results, as seen in Figure 25. There was no permanent degradation in the fuel cell, while having a slight increase in the high-density range values that were recorded after the NO contamination.

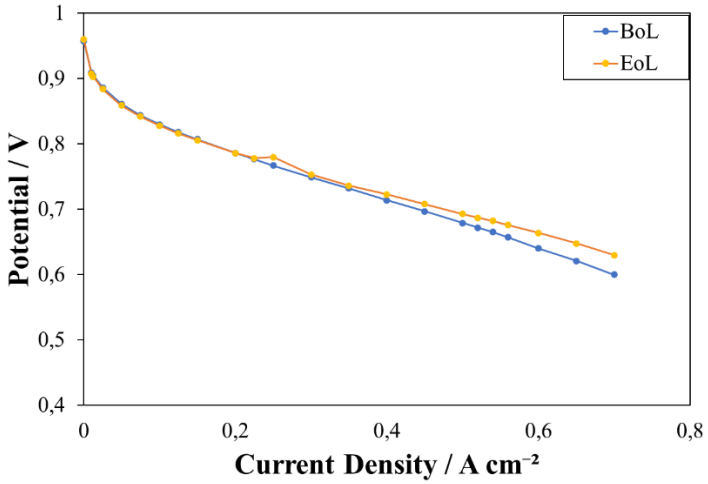

Figure 25- NO test: polarisation curve before and after NO contamination at the air inlet stream, performed at 1 A cm^{-2} feeding gases.

The EIS analysis (Figure 26), present quite interesting results; the ohmic losses show no significant variation, and the low frequency arc (mass transfer limitations) remained fairly stable throughout the contamination. However, the medium frequency arc (cathode charge transfer resistance) actually decreased after the contamination.

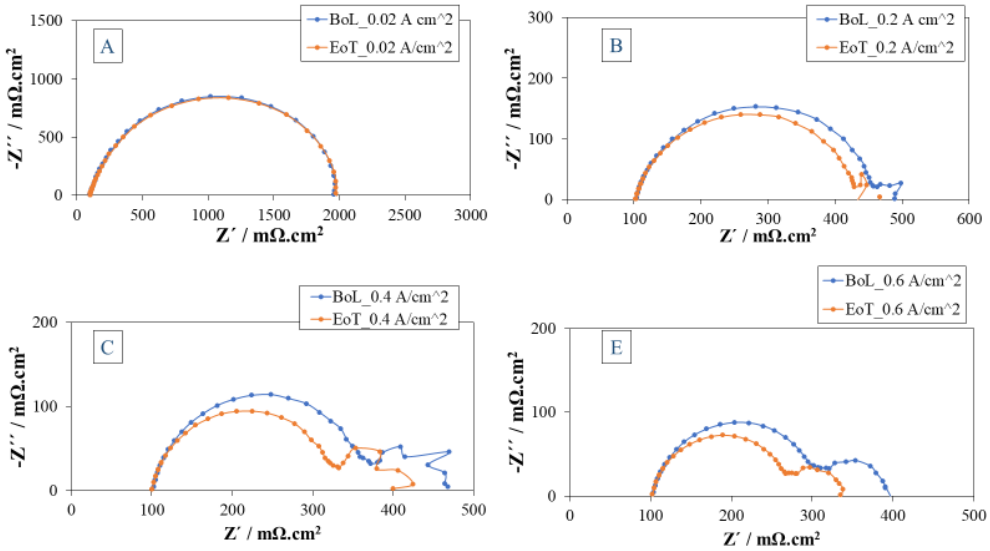

Figure 26- NO contamination: EIS Nyquist plots performed at the BoL and EoT characterisation, being performed at A) 0.02 A cm^{-2} and 50 mA amplitude, B) 0.2 A cm^{-2} and 200 mA amplitude, C) 0.4 A cm^{-2} and 500 mA amplitude, E) 0.6 A cm^{-2} and 1 A amplitude.

CV tests recorded in BoL and EoT conditions regarding NO contamination can be observed in Figure 27. ECSA declined slightly, from 13 to 12.4 mPt^2 gPt. This represents a 4 % ECSA reduction, is not significant and should account with the normal operation cell degradation.

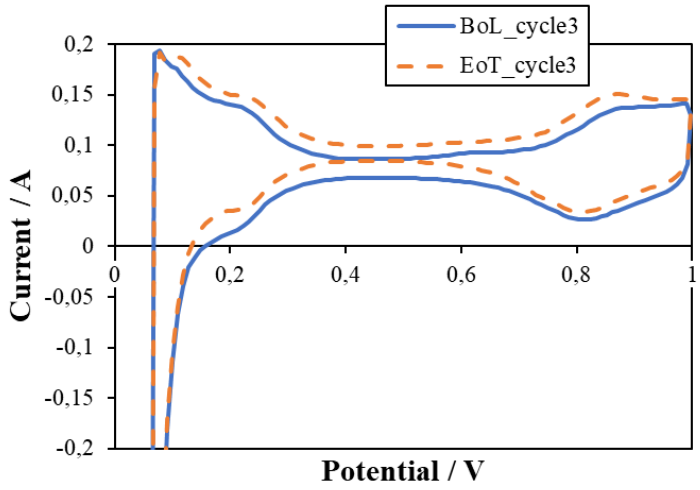

Figure 27- Cyclic voltammetry plots performed for NO contamination experiments, for the BoL and EoT. Cyclic voltammetry performed at 20 mV s^{-1} scan, with 200 mL of H_2 and N_2 feed, for the anode and cathode, respectively.

4.4 *Ex-situ* Test Analysis

4.4.1 Scanning Electron Microscopy (SEM)

Using SEM technology, samples from the membrane surface, membrane cross section and inner and outer GDL surface were scanned for particle deposits, CO migration and cross-section thickness. Due to issues in the energy-dispersive X-ray (EDX) technology in the SEM, the composition of some contaminations could not be determined.

Figure 28 show the SEM image of the cathode GDL contaminated with NaCl, its overall physical appearance is very similar to the pristine sample analysed in Annex D. Some unusual contaminations were found; however, its nature could not be determined.

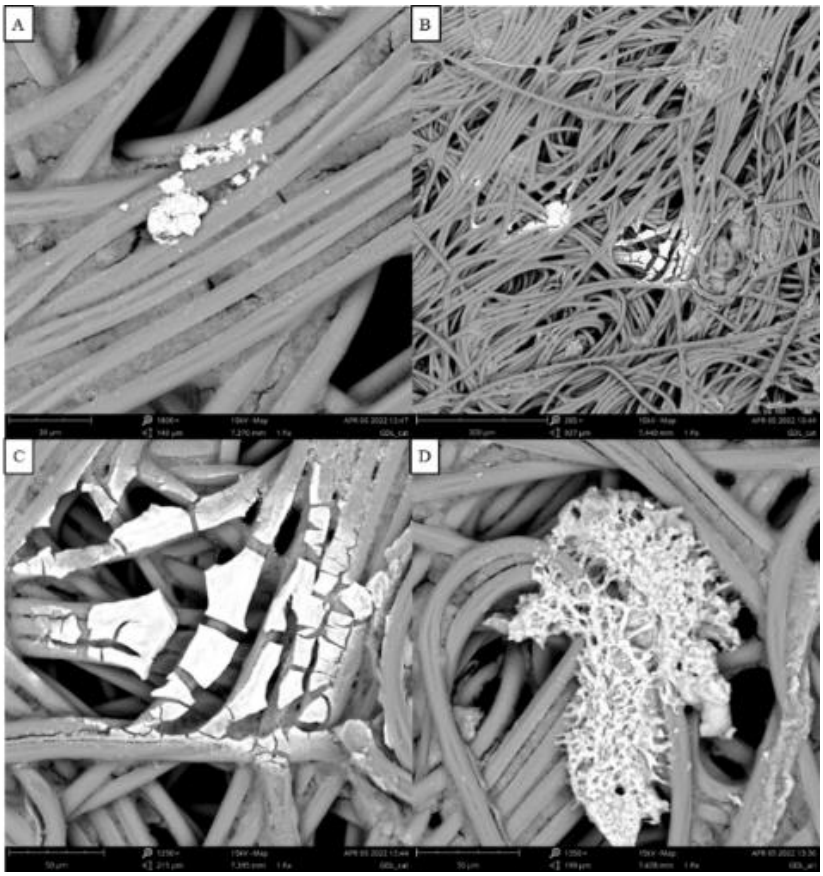

Figure 28- a, b, c, and d show different points of analysis of possible salt degradations in the cathode gas diffusion layer (GDL) in MEA1.

Figure 29, show the SEM image of the anode GDL contaminated with CO, having fibres with more degraded physical appearance, comparing with the other samples, seen in Figure D - 1, Annex D.

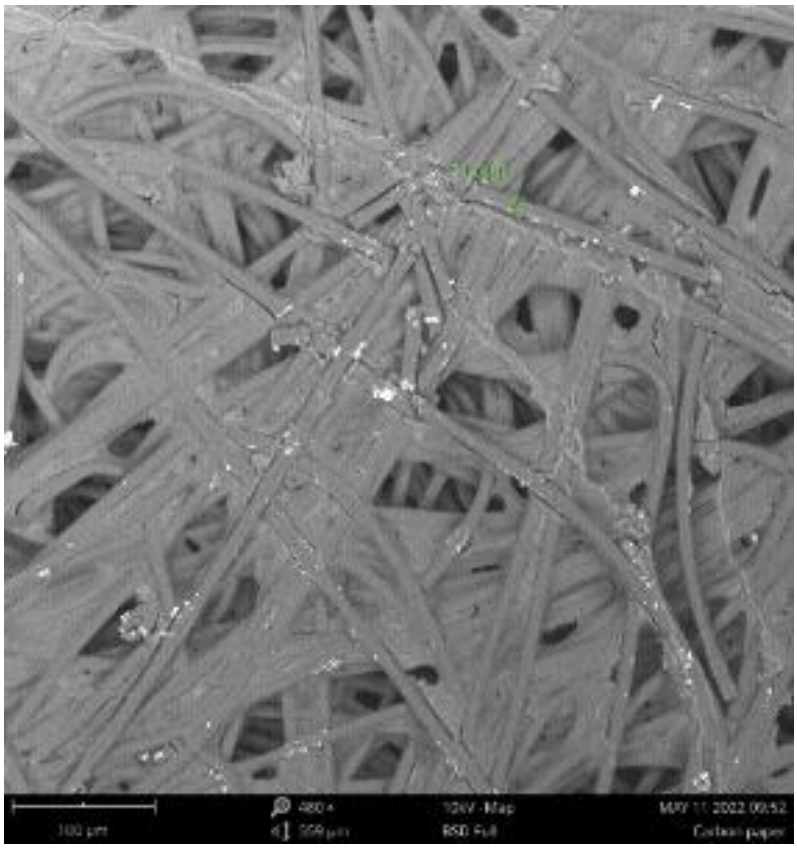

Figure 29- Anode GDL of the CO contaminated membrane.

The thickness of pristine (BoL) and contaminated (EoL) MEAs and GDL were determined from cross-section images obtained by SEM, with liquid nitrogen sample method preparation. As seen in Figure 30 and in the measurements provided in Table 5, the thickness of the membrane has not suffered significant alterations, except sample D, contaminated with CO in the air stream.

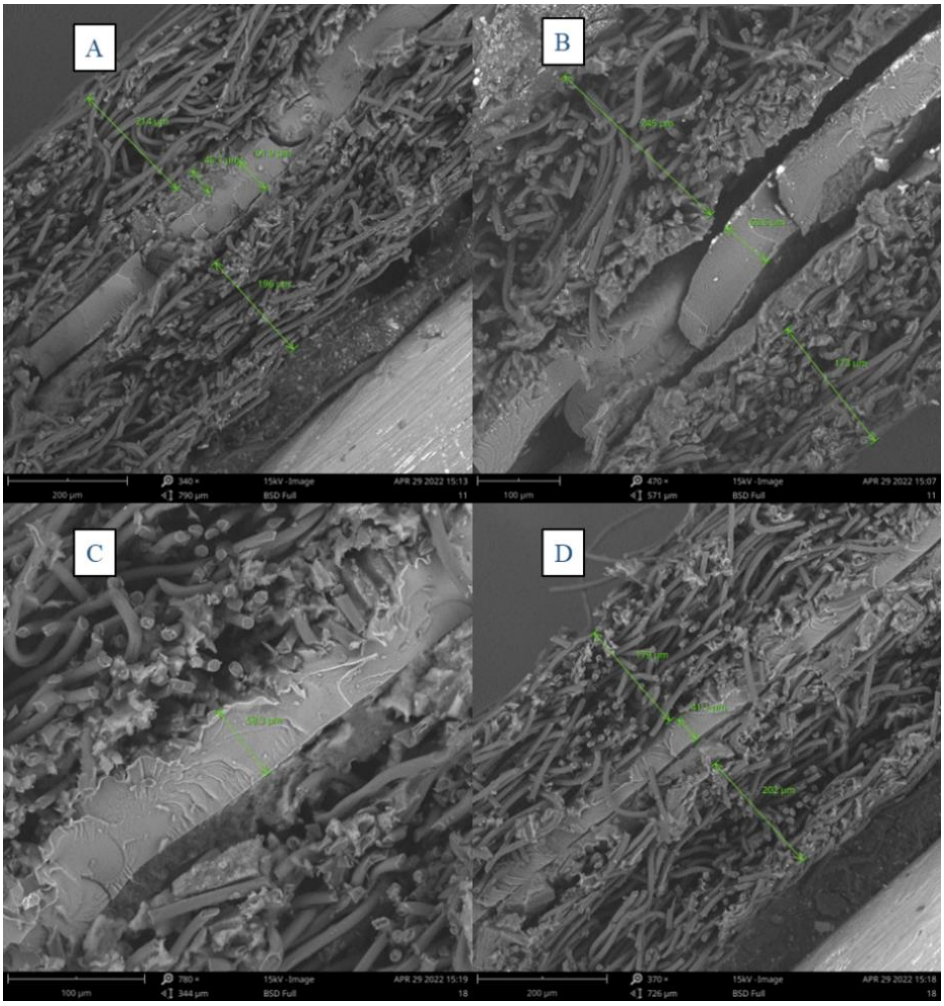

Figure 30- Cross section SEM images. Membrane, CL and GDL Thickness displayed. 340x to 780x: a) Pristine Sample. b) NaCl sample. c) Cathode CO sample 380x. d) Cathode CO sample 780x.

Table 5- Measured Membrane Thickness across samples.

Sample	Measured Membrane Thickness
Pristine (A)	61.9 µm
NaCl (B)	63.6 µm
CO 1 (C)	58.3 µm
CO 2 (D)	41.3 µm

4.4.2 Temperature Programmed Desorption (TPD)

TPD tests, paired with a mass spectrometer analysis, were conducted to detect the presence of CO molecules adsorbed in the membrane. The TPD profile results show a signal spike in each sample analysed, as seen in Figure 31.

All samples present the same profile, except the clean sample, suggesting the peak in contaminated samples was caused by CO desorption at 500 – 600 ºC and in 350 – 450 ºC. In the pristine sample, this deviation may be caused by different stages of water adsorption on the membrane. However, peak temperatures relate to the Thermo-gravimetric analysis (TGA) of a Nafion membrane and could be related to the weight loss of the sample, and not CO desorption.

As all operating conditions remained the same across samples, it is possible to associate signal intensity with CO concentration. Also, a higher CO concentration was adsorbed in the anode than in the cathode, as expected and validated by *in-situ* results, despite the much lower contamination period. It is also seen that the adsorption recorded in the GDL was significantly lower than the one present in the whole MEA, this means most CO molecules were adsorbed in the catalyst layer.

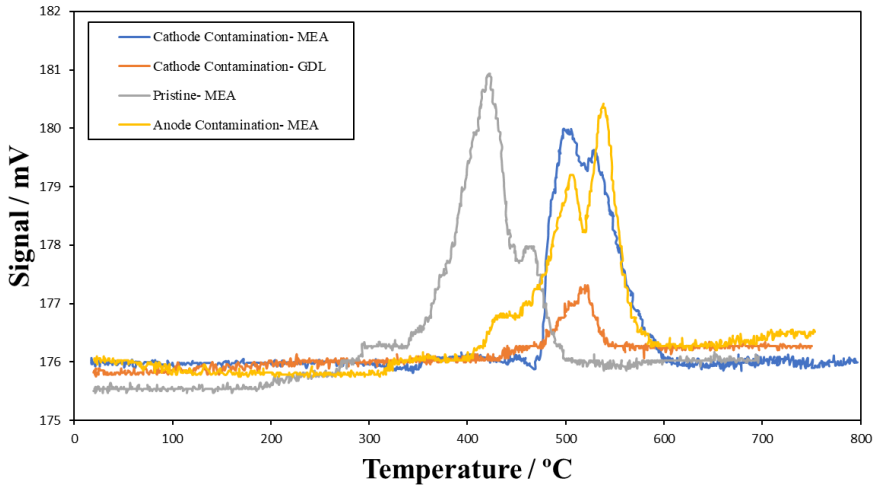

Figure 31- TPD sample test profiles referring to pristine and CO contaminations in the cathode and anode. In the caption, "Cathode/ anode contamination" and "pristine" refer to the tests elaborated on each membrane analysed in the TPD. "MEA" indications mean the whole membrane was analysed, and "GDL" indication means only the cathode side GDL composed the sample. The samples were heated at 10 º/min.

MS data in Figures 32 and 33 show no significant peak in CO. The small peaks observed in the contaminated samples (Figure 32) in temperatures similar to the ones presented in TPD results are not significant enough to point to a CO desorption at that temperature, due to the significantly low current values obtained. These could be caused by sample degradation at that temperature.

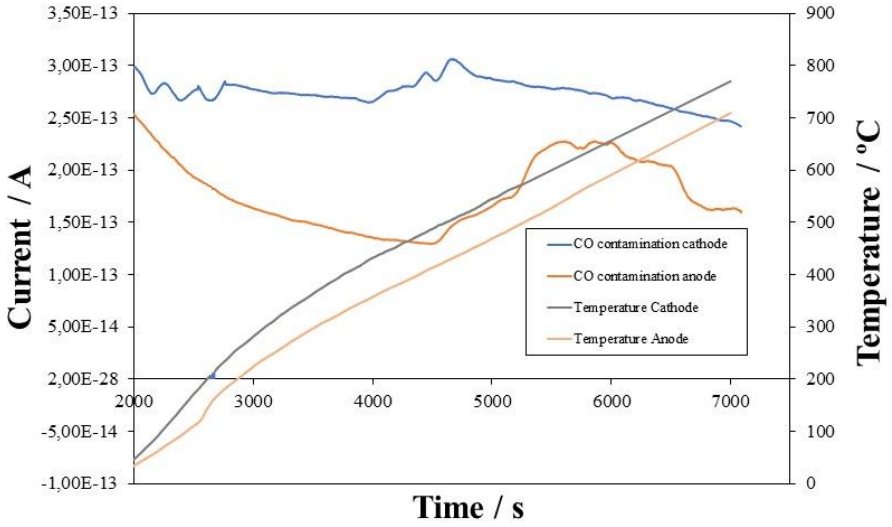

Figure 32- MS results regarding CO-contaminated samples show small peaks in temperatures similar to the obtained TPD results.

In Figure 33, it is clear that no CO was detected in the pristine sample. The perturbation at t= 4500 seconds corresponds to the disturbance seen in TPD data (Figure 31), pointing to an unknown sample degradation. Further testing would be required to determine the nature of this disturbance. However, the objective to determine that the peak not caused by CO adsorption was attained, becoming thus clear this disturbance is not very different from the other samples.

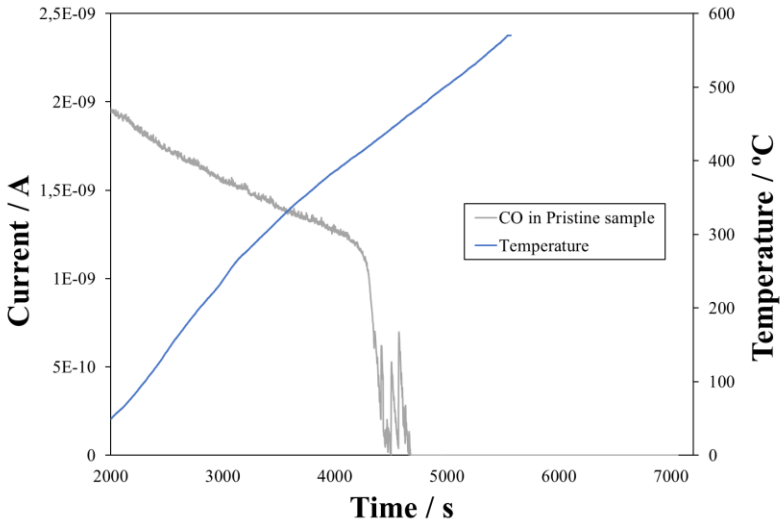

Figure 33- MS results regarding the pristine sample.

4.1.3 Inductively Coupled Plasma Mass Spectrometry (ICP-MS)

To perform the ICP analysis, the digestion conducted is specified in Section 3.3.2.3 Inductively Coupled Plasma Mass Spectrometry (ICP-MS) was conducted to liquefy the MEA sample. However, a complete dissolution of the sample was not achieved. The baseline and the contaminated samples showed similar results from the three samples tested. The Na^+ ion concentration in the samples was residual in all samples, with about 3.4 ppm concentration in the solution. This is likely to be associated with measurement errors and external contaminations. Further results can be found in Annex D.

It can be concluded from this test that no significant NaCl contamination remained in the cell after recuperation. In line with the obtained data and supporting the thesis, no permanent damage was recorded in the cell.

4.5 Result Comparison

This chapter compares the results of all the tests conducted and assessed the effects of different contaminations. The eligible parameters for this comparison were ECSA area variation, medium performance degradation rate, and polarization curves.

Figure 34 shows the mean hourly performance evolution throughout the entire contamination period for all the contaminations, as well as the baseline test referred to as Pristine. The figure is divided into fixed current tests (a) and fixed potential tests (b).

Pristine tests in both modes have shown a slight increase in performance during the 20 hours of operation. This reinforces the idea that the 20 hours of break-in procedure is not enough for the cell to reach its full potential. These values will serve as a reference for the contamination tests.

Salt tests, *NaCl 1* and *NaCl 2*, recorded in potentiostat and galvanostat mode, respectively, show equivalent results. A small recoverable degradation rate was observed in both tests, and both present a considerable degradation acceleration when compared to the respective baseline tests.

Carbon monoxide contaminations in the cathode, *CO Cathode 1* and *CO Cathode 2*, show the most extensive performance decay in the graph. *CO Cathode 1* is roughly double the rate of *NaCl 2*, conversely, *CO Cathode 2* was just 16 % more harmful than the salt test. This can be explained by the contamination time, as *CO Cathode 2* set elapsed for a total of 20 hours, and the two others for a period of 60 hours each.

Regarding anode CO contamination values, detailed in Appendix C, the degradation rates obtained in this experiment were not present in the Figure 34 graph for scale purposes. The potential evolution rate in this test was around 130 mV h^{-1}, representing by far the most aggressive contamination. Potential decay was 220 times steeper than the highest recorded in the cathode, also by carbon monoxide.

Keeping in mind that the contamination value used in the anode was equal to the intermediate one in the cathode, 50 ppm, we can conclude that the CO adsorption is much stronger in the anode. This reflects on irreversible losses demonstrated in the ECSA and polarization curves.

The Nitric Oxide set displays the lowest contamination rate of all results. A degradation rate very close to zero suggests no contamination effect on the performance. Another possible hypothesis is that even after the 20-hour activation and the 20-hour baseline test, the potential of the cell still had the tendency to keep rising, and the true degradation rate was similar in absolute

value to the ascending trend. These rates cancel each other to form the resulting potential evolution. This theory is not very probable, because activation, mainly in the 100% RH value used, should not take so much time to be completed (Tsotridis *et al*., 2015).

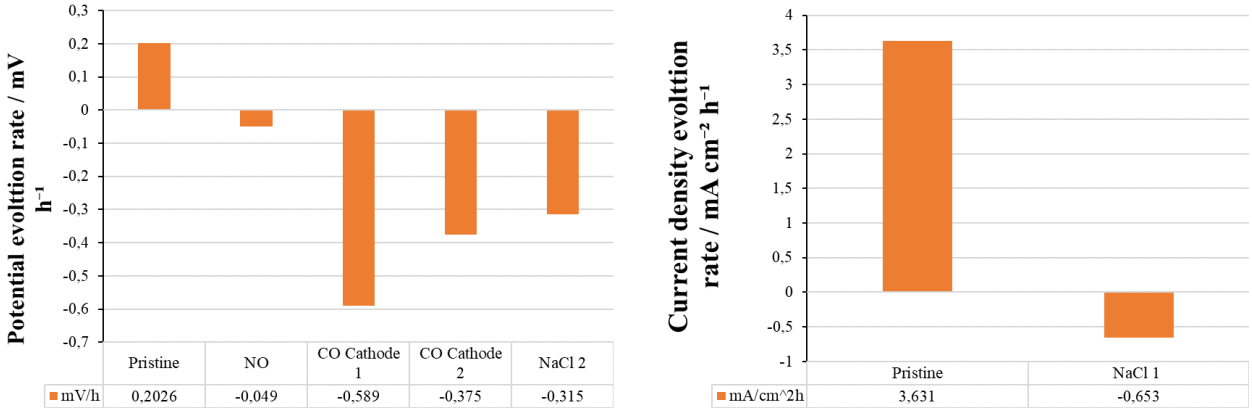

Figure 34- Comparison of the performance evolution of different test sets: a) Galvanostat mode b) Potentiostat mode

In the CV analysis, the ECSA was calculated, and the reduction of the surface area after each contamination is displayed in Figure 35 in the form of percentage. In *NO* and *NaCl 2* contaminations, a small decay can be observed due to normal cell operation, and in these sets it can be concluded that there were no significant alterations to the electrochemical surface area, and the active sites suffered minimal to no degradation.

The carbon monoxide cathode contaminations, represented by *COcat1* and *COcat2*, show an unusually large ECSA drop, and the longest contamination, *COcat1*, also suffered the most significant area drop. This suggests that some active sites might have been obstructed by CO molecules adsorption. This is validated by the decrease in the mass transport region in the I-V curves and EIS tests.

No CV tests were conducted after the CO anode contamination. This was due to the fact that the open cell voltage would not drop to <100 mV values even after 24 hours of nitrogen purging, and the CV procedure could not be initiated. A much more significant increase in ECSA after this test would be expected, as the CO adsorption is expected to be stronger in anode contaminations. This phenomenon can be seen in the I-V curves and EIS results.

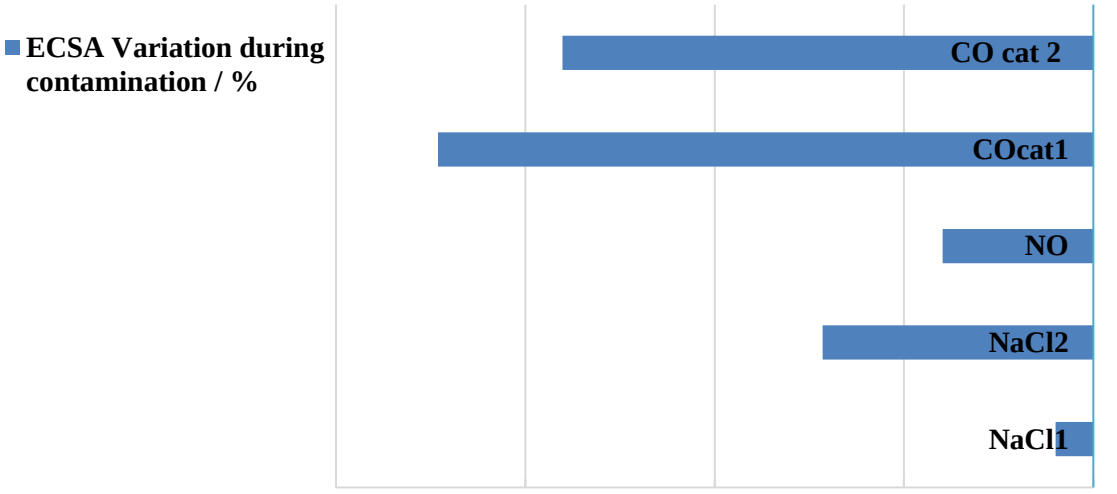

	NaCl1	NaCl2	NO	COcat1	CO cat 2
ECSA Variation during contamination / %	-1,00%	-7,15%	-3,98%	-17,31%	-14,02%

Figure 35- Comparison of the ECSA variation during all test sets.

INTENTIONALLY LEFT BLANK

Chapter 5 Conclusions and Future Work

In this chapter, the conclusions of the theoretical and experimental scopes of the study are presented, as well as recommendations for future work.

5.1 Conclusion

Fuel cell technology offers the PAF a zero-emission, high specific energy solution for UAS operation. Air contaminations in operational environments could pose a potential threat to this technology, as these cause significant degradation in the aircraft that operate in these conditions.

This thesis aimed to assess the concept of a fuel cell powered UAS adapted to the PAF requirements and test the performance of a basic fuel cell in conditions neighbouring environments of operation containing possible hazardous contaminations for its operation. This chapter summarises the results and conclusions obtained throughout the dissertation.

A literature review containing the theoretical basis of the work was elaborated. It clarified the foundation and reasoning behind the selection of this specific energy power system for PAF unmanned systems. It also comprises the working mechanisms that explain the conclusions of the subsequent chapters and the preceding work regarding the most similar contaminations in analogous operational systems and conditions.

The test bench used was adapted for the contamination tests. The operating conditions were optimised for the highest and most stable performance and the possible settings that mostly resembled the recreated environments. The Quintech membrane, Zahner load, controllers, bubblers, pumps, software, and some accessory equipment were described, as well as the reasoning behind the contamination concentrations and periods.

Regarding NaCl contamination tests, the critical factor would be the adsorption of chloride ions in the catalyst layer and subsequent reduction of active sites, causing irreversible performance loss. There is no comprehensive evidence that salt particles crossed the GDL and reached the catalyst, which indicates that the concentration of NaCl used in the experiments for this thesis does not affect the PEMFC performance.

SEM analysis has shown contaminations thought to be salt particles, but their composition could not be associated with NaCl. Instead, ICP results show no significant concentration of Na^+ in no part of the MEA, meaning all salt particles were removed during the recovery. *In situ* tests show minimal irreversible losses, likely associated with the natural decay of the cell.

Carbon Monoxide was responsible for the biggest performance losses seen in this study. Data from performance tests, polarisation curves, EIS and CV point to irreversible performance decay to some extent, caused by CO contaminations both in the cathode and in the anode.

In the cathode, concentrations presented a deterioration, varying from 0.3 to 0.5 mV h^{-1}. This value is acceptable since the operation over a wildfire is time limited. A drop in ECSA of 14 % after the test suggests a significant blockage of catalytic sites.

CO contaminations can be cumulative and irrecuperable, but it is important to remind that these results are obtained after 20 hours in the worst possible CO concentrations registered at 500 ft, followed by two 20 hours blocks in continuous feeding of concentrations four and six times the first. When translated to flight hours above a wildfire, although it cannot be accurately estimated, these test periods would amount to a sum most likely larger than the expected lifetime of most systems.

Nitrate Oxide tests led to the most curious results. The performance test displayed the most stable performance and the lowest decay rate of all contaminations. Furthermore, almost all characterization techniques pointed to a slight performance improvement after the contamination. Compared with results in the literature, this is very unexpected, and the reasoning could be related to the stoichiometry of the fed gases being much lower, the platinum loading of our MEA being higher, or the high humidity conditions in our experiment compared to some literature.

As stemmed from above, the key conclusion of this study is that for the conditions and cell used, and only concerning the cathode contaminations, no significant permanent damage was recorded in the cell for an operation time range from 15 to 60 hours. In actual drone operation above 500 ft, at least for the first 60 hours, environment causes will not produce significant and permanent degradation. However, prolonged wildfire operation may cause damage to the fuel cell, reducing ECSA over time.

It can be concluded that the main objectives of the thesis were attained. The concept of a PAF fuel cell UAS was studied and analysed in all its strands, the behaviour of a basic fuel cell under hazardous operational environments was assessed, and a foundation for future work in UAS fuel cells in the PAF was made. PEMFC application in these systems can provide a zero-emission solution while enhancing endurance and allowing rapid refuelling, being resilient, to a certain degree, to the contaminations studied.

5.2 Future Work

During the course of this dissertation, tests, tasks, and ideas were left unfinished as available time and resources were limited. This chapter showcases a series of recommendations and investigating areas that are considered to be relevant, based on the experiences obtained from this project.

One of the conclusions of this thesis is that CO contaminations in the air stream could have some short and long-term degradative effect on operating fuel cell powered UAS in proximity of wildfires, during the wildfire monitoring operations. Therefore, studying which mitigation mechanism would have the best results in diminishing this effect on drones would improve longevity and airworthiness in this recent technology.

As evaluated in the CO and NO contaminant tests differences, different wildfire gases and different concentrations have vastly distinct effects on fuel cell performance. CO and NO alone do not represent all species present in the atmosphere in a wildfire. PMs and SO_x influence analysis could enhance the comprehension of the behaviour of fuel cells in actual fires.

Finally, when the Intelligent Energy system acquisition process is completed, a benchmarking and comparison between this commercial hybrid fuel cell and a FEUP experimental fuel cell designed explicitly for UAS would allow a better understanding of the technological maturity level of each system. Ultimately developing an adaptation to integrate a contamination mitigation strategy into one of those systems.

Bibliography

Abe, J. O., Popoola, A. P. I., Ajenifuja, E., & Popoola, O. M. (2019). Hydrogen energy, economy and storage: Review and recommendation. *International Journal of Hydrogen Energy*, *44*(29), 15072–15086. https://doi.org/10.1016/j.ijhydene.2019.04.068

Ammann, A. A. (2007). Inductively coupled plasma mass spectrometry (ICP MS): A versatile tool. *Journal of Mass Spectrometry*, *42*(4), 419–427. https://doi.org/10.1002/jms.1206

Atkinson, R. W., Hazard, M. W., Rodgers, J. A., Stroman, R. O., & Gould, B. D. (2017). An Open-Cathode Fuel Cell for Atmospheric Flight. *Journal of The Electrochemical Society*, *164*(2), F46–F54. https://doi.org/10.1149/2.0261702jes

Bayrak, Z. U., Kaya, U., & Oksuztepe, E. (2020). Investigation of PEMFC performance for cruising hybrid powered fixed-wing electric UAV in different temperatures. *International Journal of Hydrogen Energy*, *45*(11), 7036–7045. https://doi.org/10.1016/j.ijhydene.2019.12.214

Blanchard, D. C., & Woodcock, A. H. (1980). The Production, Concentration, And Vertical Distribution Of The Sea-Salt Aerosol. *Annals of the New York Academy of Sciences*, *338*(1 Aerosols), 330–347. https://doi.org/10.1111/j.1749-6632.1980.tb17130.x

Blanchard, D. C., Woodcock, A. H., & Cipriano, R. J. (1984). The vertical distribution of the concentration of sea salt in the marine atmosphere near Hawaii. *Tellus B*, *36B*(2), 118–125. https://doi.org/10.1111/j.1600-0889.1984.tb00233.x

Bradley, T. H., Moffitt, B. A., Mavris, D. N., & Parekh, D. E. (2007). Development and experimental characterization of a fuel cell powered aircraft. *Journal of Power Sources*, *171*(2), 793–801. https://doi.org/10.1016/j.jpowsour.2007.06.215

Büchi, F. N., Freunberger, S. A., Reum, M., & Delfino, A. (2005). *On The Efficiency Of H2 / O2 Automotive Pe Fuel Cell Systems*. 2.

Büchi, F. N., Freunberger, S. A., Reum, M., Paganelli, G., Tsukada, A., Dietrich, P., & Delfino, A. (2007). On the Efficiency of an Advanced Automotive Fuel Cell System. *Fuel Cells*, *7*(2), 159–164. https://doi.org/10.1002/fuce.200500257

Burke, K. (2003, agosto 17). Fuel Cells for Space Science Applications. 1st International Energy Conversion Engineering Conference (IECEC). 1st International Energy Conversion Engineering Conference (IECEC), Portsmouth, Virginia. https://doi.org/10.2514/6.2003-5938

Carrette, L., Friedrich, K. A., & Stimming, U. (2000). *Fuel Cells: Principles, Types, Fuels, and Applications**. 32.

Chapter 7: Fuel Cell Characterization. (2016). Em R. O'Hayre, S.-W. Cha, W. Colella, & F. B. Prinz, *Fuel Cell Fundamentals* (pp. 237–270). John Wiley & Sons, Inc. https://doi.org/10.1002/9781119191766.ch7

Chen, H., Cong, T. N., Yang, W., Tan, C., Li, Y., & Ding, Y. (2009). Progress in electrical energy storage system: A critical review. *Progress in Natural Science*, *19*(3), 291–312. https://doi.org/10.1016/j.pnsc.2008.07.014

Choudhury, A., Chandra, H., & Arora, A. (2013). Application of solid oxide fuel cell technology for power generation—A review. *Renewable and Sustainable Energy Reviews*, *20*, 430–442. https://doi.org/10.1016/j.rser.2012.11.031

Dawood, F., Anda, M., & Shafiullah, G. M. (2020). Hydrogen production for energy: An overview. *International Journal of Hydrogen Energy*, *45*(7), 3847–3869. https://doi.org/10.1016/j.ijhydene.2019.12.059

de Bruijn, F. A., Dam, V. A. T., & Janssen, G. J. M. (2008). Review: Durability and Degradation Issues of PEM Fuel Cell Components. *Fuel Cells*, *8*(1), 3–22. https://doi.org/10.1002/fuce.200700053

de Levie, R. (1999). The electrolysis of water. *Journal of Electroanalytical Chemistry*, *476*, 2.

Dyer, C. K. (2002). Fuel cells for portable applications. *Journal of Power Sources*, *106*, 4. https://doi.org/10.1016/S0378-7753(01)01069-2

E4tech. (2019). *The Fuel Cell Industry Review 2019*. https://www.e4tech.com/news/2018-fuel-cell-industry-review-2019-the-year-of-the-gigawatt.php

E4tech. (2021). *The Fuel Cell Industry Review 2020*. https://www.ap2h2.pt/download.php?id=22

EG&G Services. (2000). *Fuel Cell Handbook*. 352.

Força Aérea Portuguesa. (2013). *MFA 500-12 Visão Estratégica Para Sistemas De Aeronaves Não Tripuladas*. Ministério da Defesa Nacional.

Força Aérea Portuguesa. (2019). *Integração dos UAS nas operações de reconhecimento, vigilância e patrulhamento da força aérea—Redifinição da estratégia a médio prazo*. Ministério

da Defesa Nacional.

Franco, V., Correia, J., Caetano, J., & Felix, L. (2019). Design of a Class I Unmanned Aircraft for Maritime Surveillance. *2019 International Conference on Unmanned Aircraft Systems (ICUAS)*, 1126–1135. https://doi.org/10.1109/ICUAS.2019.8798217

Gazdzick, P., Mitzel, J., Garcia Sanchez, D., Schulze, M., & Friedrich, K. A. (2016). Evaluation of reversible and irreversible degradation rates of polymer electrolyte membrane fuel cells tested in automotive conditions. *Journal of Power Sources*, *327*, 86–95. https://doi.org/10.1016/j.jpowsour.2016.07.049

Goor, M., Menkin, S., & Peled, E. (2019). High power direct methanol fuel cell for mobility and portable applications. *International Journal of Hydrogen Energy*, *44*(5), 3138–3143. https://doi.org/10.1016/j.ijhydene.2018.12.019

Gröger, O., Gasteiger, H. A., & Suchsland, J.-P. (2015). Review—Electromobility: Batteries or Fuel Cells? *Journal of The Electrochemical Society*, *162*(14), A2605–A2622. https://doi.org/10.1149/2.0211514jes

Gupta, S. G., Ghonge, M., & Jawandhiya, P. M. (2013). Review of Unmanned Aircraft System (UAS). *SSRN Electronic Journal*. https://doi.org/10.2139/ssrn.3451039

Gur, O., & Rosen, A. (2009). Optimizing Electric Propulsion Systems for Unmanned Aerial Vehicles. *Journal of Aircraft*, *46*(4), 1340–1353. https://doi.org/10.2514/1.41027

He, C., Yu, R., Sun, H., & Chen, Z. (2016). Lightweight multilayer composite structure for hydrogen storage tank. *International Journal of Hydrogen Energy*, *41*(35), 15812–15816. https://doi.org/10.1016/j.ijhydene.2016.04.184

Holladay, J. D., Hu, J., King, D. L., & Wang, Y. (2009). An overview of hydrogen production technologies. *Catalysis Today*, *139*(4), 244–260. https://doi.org/10.1016/j.cattod.2008.08.039

Holton, O. T., & Stevenson, J. W. (2013). The Role of Platinum in Proton Exchange Membrane Fuel Cells. *Platinum Metals Review*, *57*(4), 259–271. https://doi.org/10.1595/147106713X671222

Hongsirikarn, K. (2010). *Effect Of Impurities On Performance Of Proton Exchange Membrane Fuel Cell Components*. Clemson University.

Hordé, T., Achard, P., & Metkemeijer, R. (2012). PEMFC application for aviation: Experimental

and numerical study of sensitivity to altitude. *International Journal of Hydrogen Energy*, *37*(14), 10818–10829. https://doi.org/10.1016/j.ijhydene.2012.04.085

Ishii, T., & Kyotani, T. (2016). Temperature Programmed Desorption. Em *Materials Science and Engineering of Carbon* (pp. 287–305). Elsevier. https://doi.org/10.1016/B978-0-12-805256-3.00014-3

Jiménez, S., Soler, J., Valenzuela, R. X., & Daza, L. (2005). Assessment of the performance of a PEMFC in the presence of CO. *Journal of Power Sources*, *151*, 69–73. https://doi.org/10.1016/j.jpowsour.2005.02.049

Jing, F., Hou, M., Shi, W., Fu, J., Yu, H., Ming, P., & Yi, B. (2007). The effect of ambient contamination on PEMFC performance. *Journal of Power Sources*, *166*(1), 172–176. https://doi.org/10.1016/j.jpowsour.2006.12.103

Kamarudin, S. K., Achmad, F., & Daud, W. R. W. (2009). Overview on the application of direct methanol fuel cell (DMFC) for portable electronic devices. *International Journal of Hydrogen Energy*, *34*(16), 6902–6916. https://doi.org/10.1016/j.ijhydene.2009.06.013

Kayfeci, M., Keçebaş, A., & Bayat, M. (2019). Hydrogen production. Em *Solar Hydrogen Production* (pp. 45–83). Elsevier. https://doi.org/10.1016/B978-0-12-814853-2.00003-5

Khandelwal, B., Karakurt, A., Sekaran, P. R., Sethi, V., & Singh, R. (2013). Hydrogen powered aircraft: The future of air transport. *Progress in Aerospace Sciences*, *60*, 45–59. https://doi.org/10.1016/j.paerosci.2012.12.002

Kunusch, C., Puleston, P., & Mayosky, M. (2012). PEM Fuel Cell Systems. Em C. Kunusch, P. Puleston, & M. Mayosky, *Sliding-Mode Control of PEM Fuel Cells* (pp. 13–33). Springer London. https://doi.org/10.1007/978-1-4471-2431-3_2

Lapeña-Rey, N., Blanco, J. A., Ferreyra, E., Lemus, J. L., Pereira, S., & Serrot, E. (2017). A fuel cell powered unmanned aerial vehicle for low altitude surveillance missions. *International Journal of Hydrogen Energy*, *42*(10), 6926–6940. https://doi.org/10.1016/j.ijhydene.2017.01.137

Lapeña-Rey, N., Mosquera, J., Bataller, E., & Ortí, F. (2010). First Fuel-Cell Manned Aircraft. *Journal of Aircraft*, *47*(6), 1825–1835. https://doi.org/10.2514/1.42234

Larminie, J., & Dicks, A. (2003). *Fuel cell systems explained* (2nd ed). J. Wiley.

Lee, J. K., Lee, C., Fahy, K. F., Zhao, B., LaManna, J. M., Baltic, E., Jacobson, D. L., Hussey, D. S., & Bazylak, A. (2020). Critical Current Density as a Performance Indicator for Gas-Evolving Electrochemical Devices. *Cell Reports Physical Science*, *1*(8), 100147. https://doi.org/10.1016/j.xcrp.2020.100147

Mag, P. (1889). *V. A new form of gas battery*. 9. https://royalsocietypublishing.org/doi/10.1098/rspl.1889.0036

Mikkola, M. S., Rockward, T., Uribe, F. A., & Pivovar, B. S. (2007). The Effect of NaCl in the Cathode Air Stream on PEMFC Performance. *Fuel Cells*, *7*(2), 153–158. https://doi.org/10.1002/fuce.200600206

Miranda, A. I. (2004). An integrated numerical system to estimate air quality effects of forest fires. *International Journal of Wildland Fire*, *13*(2), 217. https://doi.org/10.1071/WF02047

Miranda, A. I., Ferreira, J., Valente, J., Santos, P., Amorim, J. H., & Borrego, C. (2005). Smoke measurements during Gestosa-2002 experimental field fires. *International Journal of Wildland Fire, 14*(1), 107. https://doi.org/10.1071/WF04069

Miranda, A. I., Martins, V., Cascão, P., Amorim, J. H., Valente, J., Borrego, C., Ferreira, A. J., Cordeiro, C. R., Viegas, D. X., & Ottmar, R. (2012). Wildland Smoke Exposure Values and Exhaled Breath Indicators in Firefighters. *Journal of Toxicology and Environmental Health, Part A*, *75*(13–15), 831–843. https://doi.org/10.1080/15287394.2012.690686

Miranda, A. I., Martins, V., Cascão, P., Amorim, J. H., Valente, J., Tavares, R., Borrego, C., Tchepel, O., Ferreira, A. J., Cordeiro, C. R., Viegas, D. X., Ribeiro, L. M., & Pita, L. P. (2010). Monitoring of firefighters exposure to smoke during fire experiments in Portugal. *Environment International*, *36*(7), 736–745. https://doi.org/10.1016/j.envint.2010.05.009

Misz, U., Talke, A., Heinzel, A., & Konrad, G. (2016). Sensitivity Analyses on the Impact of Air Contaminants on Automotive Fuel Cells. *Fuel Cells*, *16*(4), 444–462. https://doi.org/10.1002/fuce.201500159

Moore, J. M., Adcock, P. L., Lakeman, J. B., & Mepsted, G. O. (2000). *The effects of battlefield contaminants on PEMFC performance*. 7.

Nagahara, Y., Sugawara, S., & Shinohara, K. (2008). The impact of air contaminants on PEMFC performance and durability. *Journal of Power Sources*, *182*(2), 422–428. https://doi.org/10.1016/j.jpowsour.2007.12.091

Ni, M., Leung, D. Y. C., Leung, M. K. H., & Sumathy, K. (2006). An overview of hydrogen production from biomass. *Fuel Processing Technology*, *87*(5), 461–472. https://doi.org/10.1016/j.fuproc.2005.11.003

Nishizawa, A., Kallo, J., Garrot, O., & Weiss-Ungethüm, J. (2013). Fuel cell and Li-ion battery direct hybridization system for aircraft applications. *Journal of Power Sources*, *222*, 294–300. https://doi.org/10.1016/j.jpowsour.2012.09.011

Oliveira, M. N. J. (2014). *O Programa De Sistemas Aéreos Não Tripulados Da Força Aérea Portuguesa Como Alicerce Da Capacidade Aérea Não Tripulada Nacional*. 107. Instituto De Estudos Superiores Militares.

Pan, Z. F., An, L., & Wen, C. Y. (2019). Recent advances in fuel cells based propulsion systems for unmanned aerial vehicles. *Applied Energy*, *240*, 473–485. https://doi.org/10.1016/j.apenergy.2019.02.079

Pérez, L. C., Koski, P., Ihonen, J., Sousa, J. M., & Mendes, A. (2014). Effect of fuel utilization on the carbon monoxide poisoning dynamics of Polymer Electrolyte Membrane Fuel Cells. *Journal of Power Sources*, *258*, 122–128. https://doi.org/10.1016/j.jpowsour.2014.02.016

Presidência do Concelho de Ministros (2020) "Resolução do Conselho de Ministros n.º 53/2020"*Diário da República, 1.ª série* 133 (julho) 2-157 https://dre.pt/dre/detalhe/resolucao-conselho-ministros/53-2020-137618093

Rayment, C., & Sherwin, S. (2003). *Introduction to Fuel Cell Technology*. Department of Aerospace and Mechanical Engineering.

Rossmeisl, J., Logadottir, A., & Nørskov, J. K. (2005). Electrolysis of water on (oxidized) metal surfaces. Chemical Physics, 319(1–3), 178–184. https*://doi.org/10.1016/*j.*chemphys*.2005.05.038

Sasank, B. V., Rajalakshmi, N., & Dhathathreyan, K. S. (2016). Performance analysis of polymer electrolyte membrane (PEM) fuel cell stack operated under marine environmental conditions. Journal of Marine Science and Technology, 21(3), 471–*478. https://doi.org/*10.1007/s00773-016-0369-y

Smirnov, A., Holben, B. N., Eck, T. F., Dubovik, O., & Slutsker, I. (2003). Effect of wind speed on columnar aerosol optical properties at Midway Island: EFFECT OF WIND SPEED ON *MARITIME AEROSOL*. *Journal* of Geophysical Research: Atmospheres, 108(D24), n/a-n/a. https://doi.org/10.1029/2003JD003879

St-Pierre, J. (2011). PEMFC contamination model: Foreign cation exchange with ionomer protons. Journal of Power Sources, 196(15), 6274–6283. https://doi.org/10.1016/j.jpowsour.2011.04.008

St-Pierre, J., Angelo, M., Bethune, K., Ge, J., Higgins, S., Reshetenko, T. V., Virji, M. B. V., & Zhai, Y. (2014). *PEMFC Contamination—Fundamentals and Outlook. ECS Transactions, 61(23), 1–14*. https://doi.org/10.1149/06123.0001ecst

Swider-Lyons, K., Stroman, R., Page, G., Schuette, M., Mackrell, J., & Rodgers, J. (2011, setembro 21). Hydrogen *Fule Cell Propulsion for Long* Endurance Small UVAs. AIAA Centennial of Naval Aviation Forum «100 Years of Achievement and Progress», Virginia Beach, VA. https://doi.org/10.2514/6.2011-6975

Talke, A., Misz, U., Konrad, G., & Heinzel, A. (2018). Influence of Nitrogen Compounds on PEMFC: A Comparative Study. *Journal of The Electrochemical* Society, 165(6), F3111–F3117. https://doi.org/10.1149/2.0181806jes

Tanksale, A., Beltramini, J. N., & Lu, G. M. (2010). A review of catalytic hydrogen production processes from biomass. Renewable *and Sustainable* Energy *Reviews*, 14(1), 166–182. https://doi.org/10.1016/j.rser.2009.08.010

Tiimus, K., Murumäe, M., Väljaots, E., & Tamre, M. (2015). High-Efficiency Internal Combustion Engine Used in the Unmanned Aircraft. Solid State Phenomena, 220–221, 928–933. https://doi.org/10.4028/www.scientific.net/SSP.220-221.928

Turpin, C., Morin, B., Bru, E., Rallieres, O., Roboam, X., Sareni, B., Garcia Arregui, M., & Roux, N. (2017). Power for Aircraft Emergencies*: A Hybrid Proton-Exchange Membrane* H2\/O2 Fuel Cell and Ultracapacitor System. IEEE Electrification Magazine, 5(4), 72–85. https://doi.org/10.1109/MELE.2017.2758879

Uddin, M. A., Qi, J., Wang, X., Pasaogullari, U., & Bonville, L. (2015). Distributed cation contamination from cathode to anode direction in *polymer electrolyte* fuel cells. International Journal of Hydrogen Energy, 40(38), 13099–13105. https://doi.org/10.1016/j.ijhydene.2015.07.134

Uemura, S., Yamazki, M., Yoshida, T., Jao, T.-C., & Hirai, S. (2017). Performance Degradation of PEMFC by Sea Salt Aerosol Contamination. ECS Transactions, 80(8), 651–655. *https://doi.org/10.*1149/*08008*.0651ecst

Valdés-López, V. F., Mason, T., Shearing, P. R., & Brett, D. J. L. (2020). Carbon monoxide poisoning and mitigation strategies for polymer electrolyte membrane fuel cells – *A review*. *Progress in* Energy *and* Combustion Science, 79, 100842. https://doi.org/10.1016/j.pecs.2020.100842

Valente, J., Miranda, A. I., Lopes, A. G., *Borrego, C.*, *Viegas*, *D*. X., & Lopes, M. (2007). Local-scale modelling system to simulate smoke dispersion. International Journal of Wildland Fire, 16(2), 196. https://doi.org/10.1071/WF06085

Verstraete, D. (2013). Long range transport aircraft using hydrogen fuel. International *Journal of Hydrogen Energy*, 38*(*34), 14824–14831. https://doi.org/10.1016/j.ijhydene.2013.09.021

Weiner, S. C. (2014). Advancing the hydrogen safety knowledge base. International Journal of Hydrogen Energy, 39(35), 20357–20361. https://doi.org/10.1016/j.ijhydene.2014.08.001

Yan, W.-M., Chu, H.-S., Liu, Y.-L., Chen, F., & Jang, J.-H. (2011). Effects of *chlorides on the performance of* proton *exchange* membrane fuel cells. International Journal of Hydrogen Energy, 36(9), 5435–5441. https://doi.org/10.1016/j.ijhydene.2011.01.158

Yang, C., Moon, S., & Kim, Y. (2016). A fuel cell/battery hybrid power system for an unmanned aerial vehicle. Journal of Mechanical Science and Technology, 30*(5)*, *2379*–2385. https://doi.org/10.1007/s12206-016-0448-3

Yuan, X.-Z., Li, H., Zhang, S., Martin, J., & Wang, H. (2011). A review of polymer electrolyte membrane fuel cell durability test protocols. Journal of Power Sources, 196(22), 9107–9116. https://doi.org/10.1016/j.jpowsour.2011.07.082

APPENDIX A – Stack Testbench Assembly

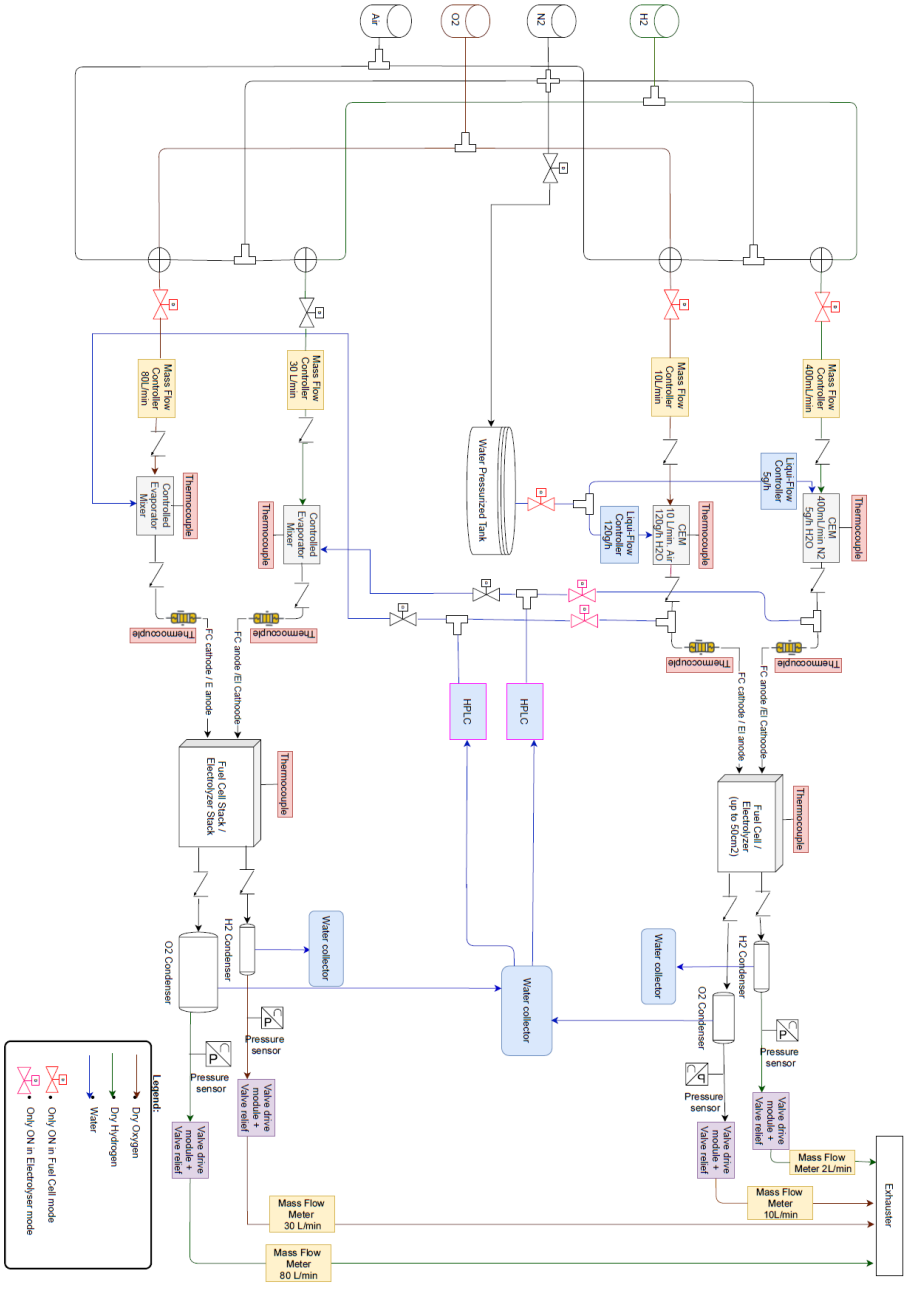

Figure A- 1 Diagram of the test bench being assembled in FEUP, operated in both fuel cell and electrolyser mode, for single cell and stack.

At the start of the experimental stage of the thesis, a new testing stand for fuel cells and electrolysers was implemented in the Laboratory for Process Engineering, Environment, Biotechnology and Energy (LEPABE) at FEUP. This subchapter presents the implementation scheme and describes the configuration and functions of the system.

As seen in Figure A- 1, the stand divides into two sections. One is suited to test stacks, the other individual cells. The layout of these sections is similar, although the latter has significantly lower gas flow rates. This system can test electrolysers as well as fuel cells, through adaptations explicit in Figure A- 1.

The pipelines of the faculty directly feed AirK, O_2, H_2 and N_2, while water is obtained from tanks in the installation. The gases pass through mass flow controllers, then enter controlled evaporator mixers (CEM), where the gas is humified. After that, gases are sent to the fuel cell, where energy outputs are monitored and controlled through a PP240 Potentiostat. The following devices in the line are H_2 and O_2 condensers, which dry out the by-products and store the resulting water in collectors that back-feed the CEMs.

Lastly, mass flow meters and pressure sensors check the exhaust gases. Thermocouples connected throughout the installation monitor the temperature in the CEM, cell/stack, and the temperature of each gas before entering the cathode and the anode. The whole system is made with the possibility to adjust the flowing gas to N_2 for Nitrogen purging.

The system is capable of operating most in situ characterisation techniques, such as Current-Voltage Measurements (I-V curves), Electrochemical Impedance Spectroscopy (EIS), and Cyclic Voltammetry (CV), in Figure A- 2 the state of the system can be seen at the time of writing.

Figure A- 2 - Test bench that is being assembled in FEUP for testing both fuel cells and electrolyser

APPENDIX B- Additional Fuel Cell Types

Phosphoric Acid Fuel Cell (PAFC)

Phosphoric acid fuel cells were the first commercially available fuel cells. Similar to some other cells, the Phosphoric Acid Fuel Cell (PAFC) uses a proton conducting electrolyte, and the reactions that occur in the anode and cathode are the ones described in equations [2.2] and [2.3], respectively. The electrolyte is an inorganic acid, concentrated phosphoric acid (H_3PO_4). This liquid acid has a freezing temperature of 42ºC, making the cell unable to operate below this temperature, with its optimal operating temperature around 180-200ºC. The catalyst is generally platinum. Low power densities and very high cost make this type of fuel cell not commercially competitive. This can be tackled with appropriate investment and research.

Molten Carbonate Fuel Cell (MCFC)

The material used for the electrolyte is the defining characteristic of this fuel cell. Alkali metal carbonates, such as lithium and potassium, are used at the liquid stage. They form a highly conductive molten salt, permeable to CO_3^{2-} ions. The reaction occurs as demonstrated in Figure B - 1.

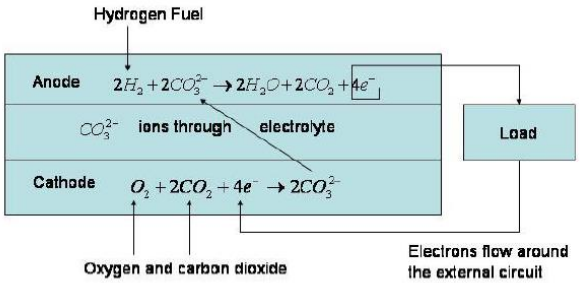

Figure B - 1 -Molten carbonate fuel cell general schematic, as per (Rayment & Sherwin, 2003)

The very high temperature of operation (600 ºC-700 ºC) brings some implications. It allows for the use of various fuels, such as carbon monoxide, and allows one of the most significant efficiencies of hydrogen fuel cells. There is no need for noble metals as catalysts at this temperature. In spite of the advantages described, the temperature of operation makes this system unsuitable for small applications

APPENDIX C- CO Anode Contamination

This set contains contamination in the hydrogen supply. It was made to analyse the differences in CO adsorption at the anode and cathode PEMFC electrodes and validate the admission method.

Initially, the cell was allowed to stabilise in 0.4 A cm^{-2}, A for 1.5 hours, then, the only contamination applied, of 50 ppm, was introduced. The response of the cell was a sharp, almost vertical, drop. This abrupt potential decrease only allowed the contamination to go on for approximately one minute. The contamination was then removed to prevent irreversible membrane failure. Consecutively, anode recovery was started at normal operation conditions with pure hydrogen; however, as no significant potential evolution was observed, the load was shut down at t = 2 h.

Between the grey and blue lines at t = 2 h, in Figure C-1, a long stop was made, in which nitrogen purging allowed a full potential recovery. Three more contaminations were introduced after one hour of pure hydrogen feed in the same conditions described before. Pure hydrogen feed allowed a steady potential recovery between these contaminations, contrary to what occurred in the first contamination.

In the last contamination, at t = 4 h, in order to prevent a possible CO controller flow overshoot, the contamination was introduced very gradually, enabling a contamination period of 15 minutes without dropping below the 0.30 V safety margin. After 8 minutes of contamination, the potential reached a level of constant voltage at a value of 0.36 V. A standard recovery then followed, slower and more unstable than the others, due to the prolonged contamination time. CO adsorption is more critical at the anode side, leading to an immediate and drastic performance drop, which was not verified on the cathode side (see subsection 4.3.1.).

From the studies conducted by Pérez *et al* ., (2014), it was observed that CO contamination on the anode caused an immediate reaction in performance. However, in the bibliography the results are not as abrupt as the ones presented in Figure C-1. TPD analysis, present in subsection 4.4.2., show that the CO adsorption was stronger in the anode electrode

sample analysed. There is a greater peak corresponding to the intensity of the CO desorbed, at an increased temperature, when comparing with the other samples.

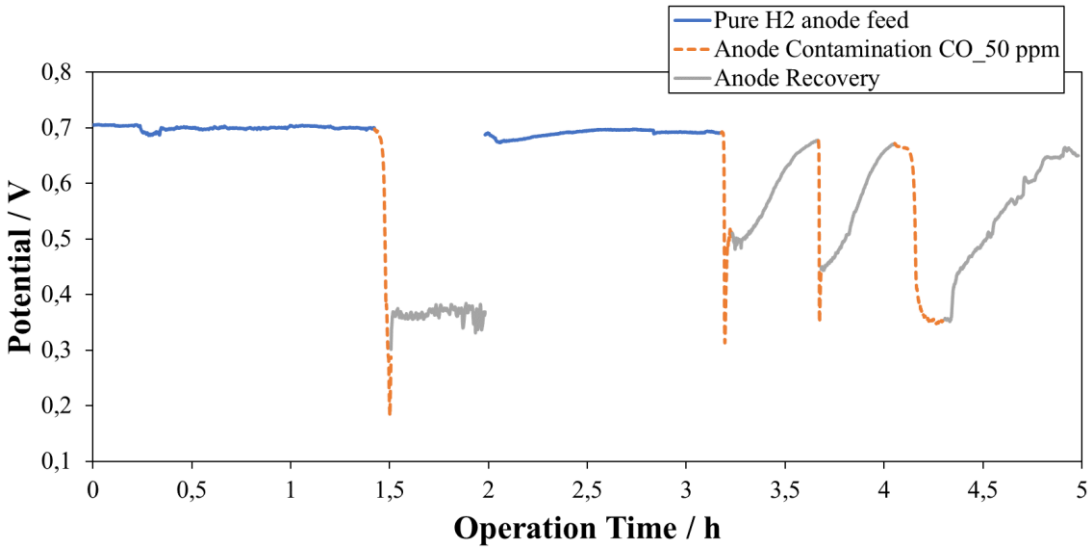

Figure C - 1- Anode CO contamination: potential vs operation time for fixed 0.4 A cm^{-2} current density with 50 ppm periodic CO contamination injection in the anode.

Regarding the characterisation, BoL and EoT tests was performed before and after the CO anode injection, to analyse performance decay and catalyst poisoning. All characterisation techniques were recorded using the operating conditions specified in Table 4. The EoT characterisation set was recorded in clean air conditions.

Observing the characterisation results, it is clear that the low exposure time to CO in the anode had evident and irreversible effects on performance. These irreversible effects can be attributed to the adsorption of CO onto the anode catalytic sites. The polarisation curve, plotted in Figure C-2, shows degradation in all ranges except in the activation area. For the maximum current density of 0.7 A cm^{-2}, the non-recuperable loss of potential was of 11 % (the potential decayed from 0.60 V to 0.54 V). At 0.4 A cm^{-2}, representative of the ohmic region, the potential decayed from 0.72 V to 0.69 V.

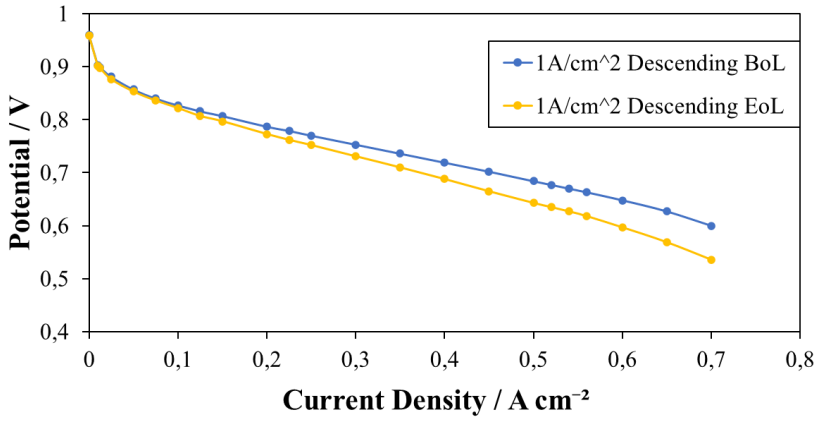

Figure C - 2- CO anode contamination: Descending Polarisation curve performed at the BoL and EoT, at 1 A cm^{-2} feeding gases.

The EIS section of the characterisation revealed pertinent results, seen in Figure C-3. The y=0 value increased roughly from 100 to 110 mΩ cm² in all plots analysed, showing an increase in ohmic losses in this contamination, which was also verified in the polarization curves in Figure C-2. This increase in ohmic resistance might have been due to ionomer degradation, which hinders the transport of protons. Impurities´ deposition on the membrane, as result of polytetrafluoroethene (PTFE) degradation from the GDL, are seen as possible sources of increased ohmic resistance

The first arc also suffered deviations throughout the contamination, having its size increased across all tests. For EIS A), representative of the kinetic region, and being performed at 0.02 A cm^{-2}, the total resistance increased in 137 mΩ cm². The second arc also increased in size, visible in EIS C) and E), in values of 240 and 25 mΩ cm², respectively. These results show a significant increase in charge transfer and mass transport resistance for this contamination.

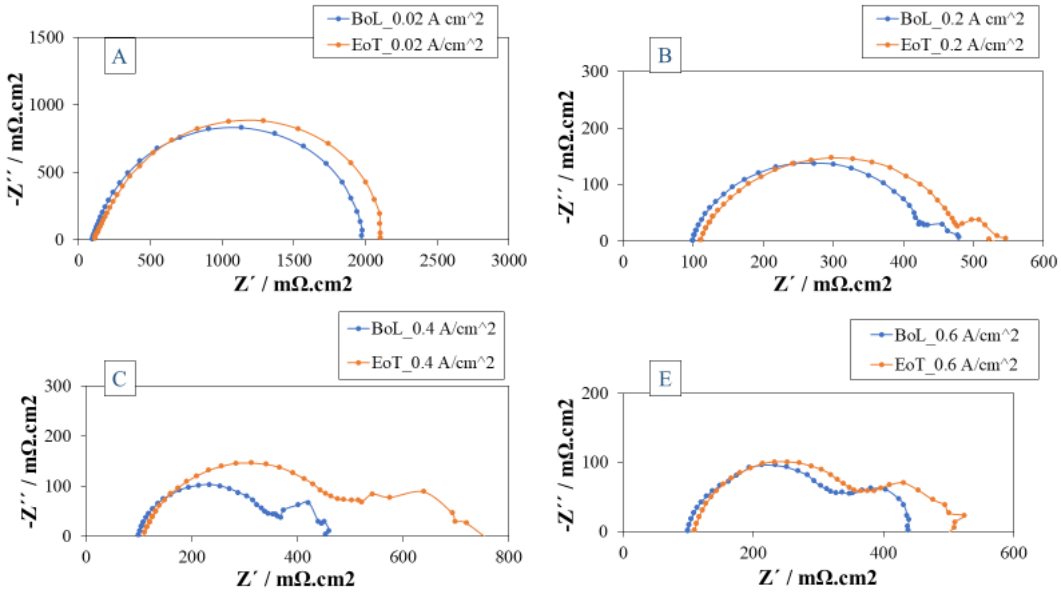

Figure C - 3- CO anode contamination: EIS Nyquist plots performed at the BoL and EoT characterisation, being performed at A) 0.02 A cm^{-2} and 50 mA amplitude, B) 0.2 A cm^{-2} and 200 mA amplitude, C) 0.4 A cm^{-2} and 500 mA amplitude, E) 0.6 A cm^{-2} and 1 A amplitude

ANNEX D – SEM Results

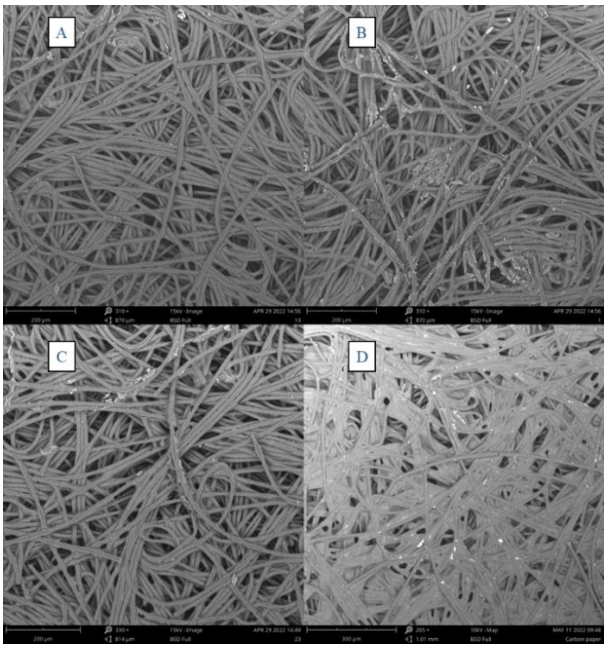

Figure D - 1 Gas Diffusion Layer SEM images. 265x to 310x: a) Pristine Sample. b) NaCl sample. c) Cathode CO sample. d) Anode CO sample

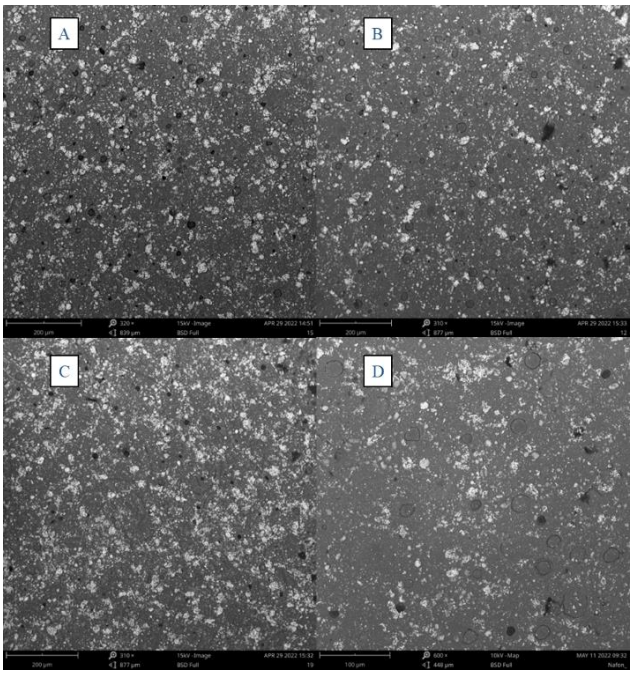

Figure D - 2 Catalyst Layer SEM images. 310x to 600x: a) Pristine Sample. b) NaCl sample. c) Cathode CO sample. d) Anode CO sample

ANNEX E – Complementary Tests

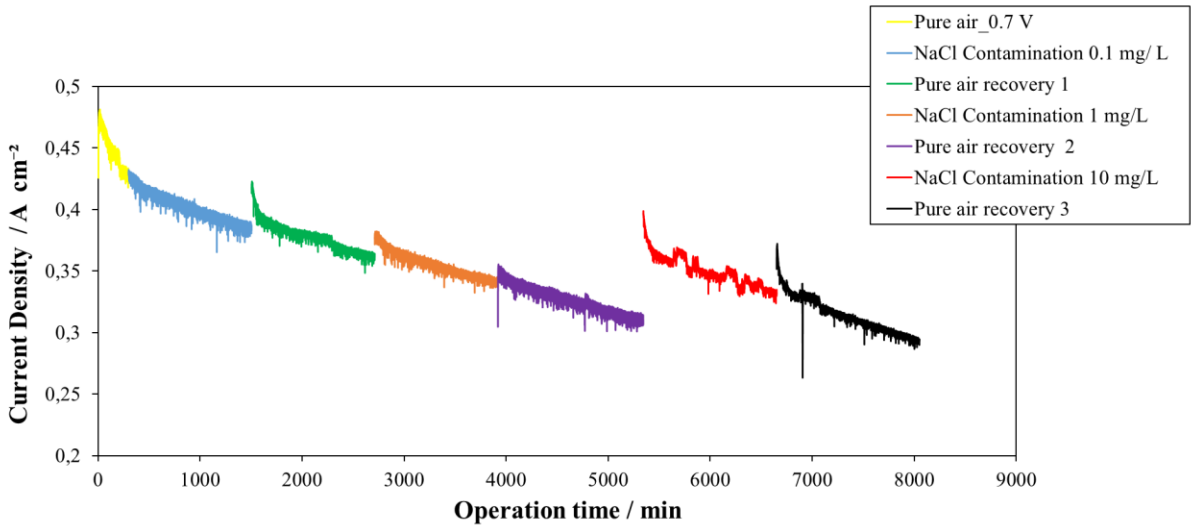

Figure E - 1 First conducted NaCl contamination test set, not used for this thesis due to experimental installation instability

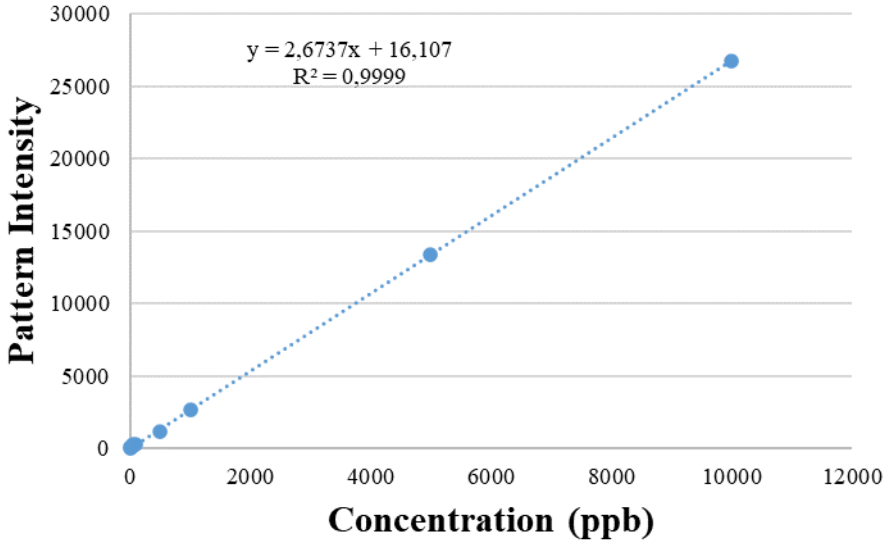

Figure E - 2- ICP test plot

ANNEX F – Polarization Curve by Quintech

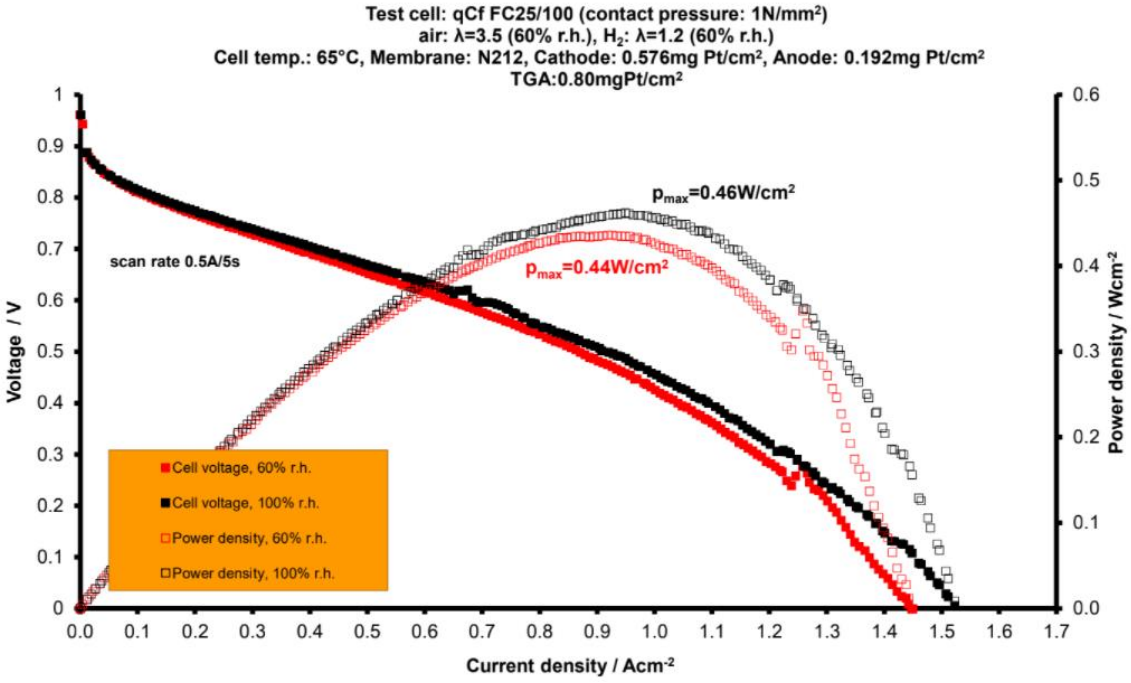

Figure F - 1 Expected polarisation curve and optimal conditions (Quintech)